



Original Paper

# Petrophysical Characterization of the Turonian and Cenomanian Intervals in the Abu Gharadig Field, Western Desert, Egypt: Inferences on Reservoir Quality and Resource Development

Sherif Farouk,<sup>1</sup> Souvik Sen ,<sup>2,5</sup> Hesham Abuseda,<sup>3</sup> Yasmien El-Shamly,<sup>4</sup>  
Alaa Salam,<sup>4</sup> and Mohamed Mahmoud Elhossainy<sup>4</sup>

Received 19 September 2021; accepted 11 April 2022  
Published online: 2 May 2022

Characterization of reservoir petrophysical properties provides critical insights into reservoir deliverability and field development strategy. The main objective of this work is to present a comprehensive core-based petrophysical assessment of the Cenomanian Bahariya Formation and the Turonian Abu Roash (AR-D and AR-E, respectively) Members of the Abu Gharadig field situated in the Western Desert, Egypt. The AR-D is water-wet and consists of micro- to mesoporous shallow marine limestone lithofacies with moderate porosity ( $\Phi$ ), poor horizontal permeability ( $Kh$ ) with poor permeability anisotropy due to the presence of vertical fractures, while the nano- to mesoporous argillaceous limestone lithofacies is very tight. Both the lithofacies exhibit primary and secondary depositional fabrics. Overall, the AR-D member exhibits impervious to poor reservoir quality, and so a suitable stimulation strategy will be essential to produce from this interval. The AR-E interval implies a tidal depositional environment. The calcareous sandstone lithofacies of the AR-E is macro- to megaporous and exhibits moderate to high porosity ( $> 15\%$ ) and excellent permeability (up to 305 mD). The meso- to microporous glauconitic siltstones of the AR-E have poor porosity and permeability. Both lithofacies are characterized by high water saturation, preserve primary depositional fabrics and consist of isotropic pore system along with some connected horizontal pores yielding higher permeability anisotropy. The Bahariya Formation consists of fine to medium grained massive sandstone lithofacies with minor siltstone intercalations, indicating a channel deposit in a coastal or fluvio-deltaic environment. It exhibits high porosity ( $\sim 20\%$ ) and permeability (up to 649 mD) but shows very high water saturation. It preserves the primary depositional fabrics with isotropic pore system. The thin siltstone intercalations may act as vertical barriers. Based on the petrophysical assessment, we made recommendations on the reservoir development aspects.

<sup>1</sup>Exploration Department, Egyptian Petroleum Research Institute (EPRI), 1 Ahmed El-Zomor Street, Nasr City, Cairo, Egypt.

<sup>2</sup>Geologix Limited, Dynasty Building, Wing A, Level 4, Andheri Kurla Road, Andheri (E), Mumbai, Maharashtra 400059, India.

<sup>3</sup>Production Department, Egyptian Petroleum Research Institute (EPRI), 1 Ahmed El-Zomor Street, Nasr City, Cairo 11727, Egypt.

<sup>4</sup>Geology Department, Faculty of Science, Kafrelsheikh University, Kafrelsheikh 33516, Egypt.

<sup>5</sup>To whom correspondence should be addressed; e-mail: souvikseniitb@gmail.com

**KEY WORDS:** Petrophysical characterization, Reservoir quality, Permeability anisotropy, Bahariya, Abu Roash.

## INTRODUCTION

The Western Desert contributes to more than one-third of Egypt's hydrocarbon production (EGPC, 2019), primarily from the Late Cretaceous clastics and carbonates of the Mesozoic rift basins. Majority of the proven hydrocarbon reserves are concentrated in the Abu Roash and Bahariya Formations. The Western Desert has always remained the key area of interest for exploration and development.<sup>1</sup> The enthusiasm has been intensified with the latest discovery in exploratory well SEMZ-11X, which delivered a 65-ft of pay zone in Cretaceous sandstones and tested with an oil production rate of 2100 bopd (barrel oil per day) without water (Apex International Energy, 2021). This indicates a lot of yet untapped hydrocarbon potential in the unexplored or less-explored areas of the Western Desert, and the newly offered hydrocarbon blocks in the 2021 bid rounds also indicate the same (EUG, 2021).

This work concentrates on the Abu Gharadig field situated in the prolific Abu Gharadig Basin (AGB) producing from the Upper Turonian and Cenomanian intervals (El Gazzar et al., 2016; Hewaidy et al., 2018). The AR-E, AR-G and Bahariya shales are the primary source rocks consisting of Types I–II kerogens (Khaled, 1999). Sarhan (2017) and Sarhan and Collier (2018) discussed the tectonics and distribution of faults of the Abu Gharadig field using 2D seismic data. Several researchers have worked on the characterization of various Cretaceous intervals from this field; e.g., Hewaidy et al. (2018) interpreted the lithofacies distribution and depositional environment of the AR-E Member using well logs, biostratigraphy and thin section petrography. Abdelmaksoud et al. (2019a, b) presented a three dimensional well log-based petrophysical, facies and structural modeling of the Upper Bahariya Formation. Sarhan (2021) presented a geophysical appraisal of the AR-C and AR-E sandstones to interpret well log-based petrophysical properties; Elhossainy et al. (2021) focused on the sedimentological and petrophysical characterization of the Bahariya Formation. However, a detailed

core-based petrophysical characterization and reservoir quality assessment of the Late Cretaceous intervals from the Abu Gharadig field is lacking, which sets the premise of this work.

The principal objectives of this paper are to: (a) identify various lithofacies from the cores and interpret their porosity, grain density, horizontal and vertical permeability behavior using the core-based measurements; (b) interpret permeability anisotropy of the reservoirs; and (c) assess reservoir quality parameters. We have integrated routine and special core analyses, wireline logs and various available drilling data and downhole measurements to achieve the objectives. This work focuses on the Bahariya Formation and the AR-E Member, which are the primary producers, as well as the AR-D carbonate interval, which has a significant reservoir potential in the Abu Gharadig field. Recently, the AR-D interval has been brought into production after successful stimulation program (Khaldia Petroleum Company, 2013). Based on the sedimentary structures and lithofacies assemblages observed in the cores, we have inferred the possible depositional environments of the reservoirs. We also discuss inferences on reservoir development strategies. The outputs of this work provide a better insight into the storage capacity and hydraulic flow potential of the studied reservoirs and will enable the subsurface exploration community to optimize their exploration and development strategies accordingly.

## Geological Settings

The AGB is an elliptical shaped E–W-trending intra-cratonic Mesozoic rift basin situated in the Northwestern Desert of Egypt (El Gazzar et al., 2016). The Qattara Ridge and Sharib–Sheiba Ridge separate it from the northern rift basins while the Sitra platform and Kattaniya Ridge mark its southern and southeastern boundary (Mahmoud et al., 2019) (Fig. 1). The Abu Gharadig area is significantly crossed by regional fault systems which are principally oriented in the NE–SW, E–W and WNW–ESE directions (Guiraud & Bosworth, 1997; Guiraud, 1998; Guiraud et al., 2005; Bosworth et al.,

<sup>1</sup> 1 mD (millidarcy) =  $9.86923 \times 10^{-16}$  meter<sup>2</sup>.

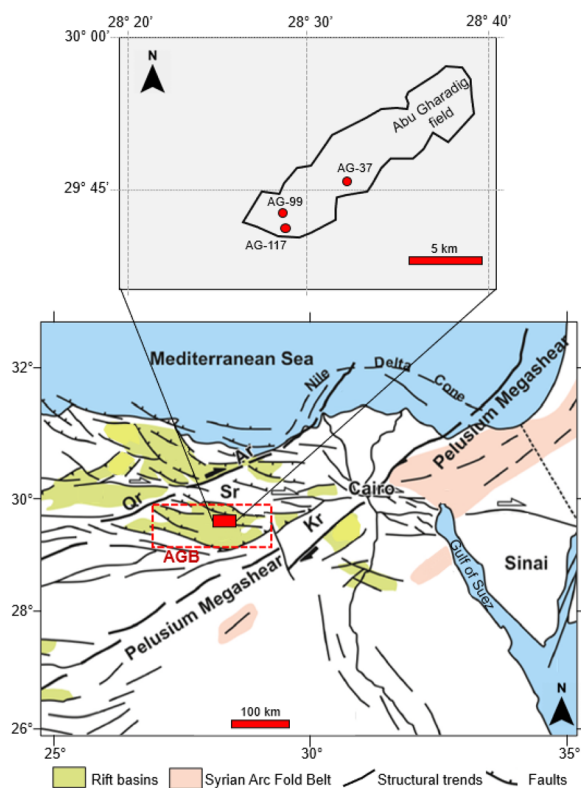


**Figure 1.** Location map of the studied Abu Gharadig field in the Abu Gharadig Basin (AGB), Western Desert along with the studied wells (AG-37, AG-99 and AG-117), and major structural features (Qr = Qattara Ridge, Sr = Sharib-Sheiba Ridge, Kr = Kattaniya Ridge) (EGPC, 1992; Bosworth et al., 2008).

2008; Moustafa, 2008). The Late Jurassic to Early Cretaceous rifting created various E–W and ENE–WSW trending half grabens including the AGB along the Northern African margin and within the intraplate region (Guiraud & Maurin, 1992). The rifting ceased during the Late Cretaceous and the basin experienced a NW–SE compression (during the Alpine orogeny), which continued through the Tertiary (Moustafa 2008; Sarhan, 2017). The effect of this compression and shortening was mainly in the northern part of the AGB (Bosworth et al., 2008). The tilting and basin inversion was responsible for creating the major structural traps in the Western Desert (Sarhan & Collier, 2018). Moustafa (2013) interpreted that AGB anticlinal traps might be formed due to the rifting related subsidence.

The studied Abu Gharadig field is the first massive hydrocarbon discovery in the central part of the AGB (El Gazzar et al., 2016). It is situated within 28.2°–28.5°E and 29.35°–30°N. It covers

roughly 60 km<sup>2</sup> and hosts roughly 12,000 ft of mixed siliciclastic and carbonate sediments of Cretaceous to Paleogene age. A regional stratigraphic sequence is presented in Figure 2 along with the formation thicknesses as encountered in the studied wells. A regional unconformity marks the boundary between the Paleogene and Mesozoic strata (Sarhan et al., 2017a, 2017b; Sarhan & Collier, 2018). The post-rift sediments of Late Cretaceous age represent major transgressive cycles with minor interruptions by shorter regressive cycles (Mansour et al., 2020). The AR was subdivided into seven distinct members, marked as A–G. Researchers have interpreted that the AR-F limestone is the main source rock in the AGB with up to 7% total organic carbon (TOC) content (Adly et al., 2016; Ghassal et al., 2018). The Cenomanian Bahariya Formation, Upper Turonian AR-C and AR-E Members are the primary reservoirs of the Abu Gharadig field. Both the AR-C and AR-E are dominated by sandstone, siltstone and shale intercalations along with minor limestones. The AR-D and AR-E also possess reservoir potential. The AR-D is limestone-dominated with minor shale interbeds, while the AR-E consists both clastics and carbonates.

## MATERIALS AND METHODS

Based on the availability of the core data, three vertical wells were chosen for this work, namely AG-117, AG-37 and AG-99. Well AG-117 was drilled to the top of the Bahariya Formation in 2013 targeting the AR-D carbonate intervals. AR-D was encountered within 9182–9545 ft<sup>2</sup> depth. A cumulative of 59 ft was cored (9403–9462 ft), and detailed measurements were performed on 88 samples in the core laboratory. The reservoir section is hydrostatically pressured ( $\sim 0.43$  psi/ft<sup>3</sup>), and a mud pressure gradient of 9.5–9.6 PPG<sup>4</sup> was maintained while drilling this formation. Well AG-37 was drilled until the AR-E in 2011. AR-E was encountered within 10,496–10,988 ft depth. A 70-ft core was recovered from the Turonian Upper AR-E Member (10,560–10,630 ft) and 71 samples were selected for core-based measurements. Mud logging data report light brown patchy oil staining and dull oil fluorescence in

<sup>2</sup> 1 ft = 0.3048 m.

<sup>3</sup> 1 psi/ft = 22.6206 Megapascal/kilometer.

<sup>4</sup> 1 PPG (pounds per gallon) = 0.12 gm/cm<sup>3</sup>.

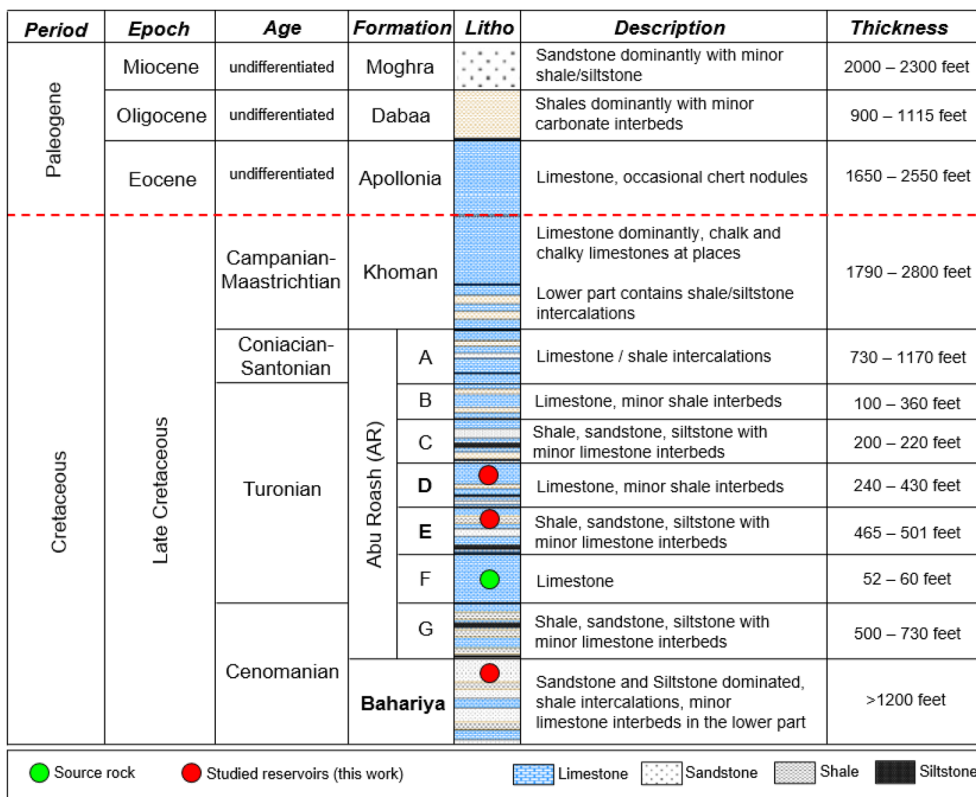


**Figure 2.** Stratigraphic column of the Abu Gharadig Basin, Western Desert, as encountered in the three studied wells. Rock units and their ages are adopted after Lotfy (1984). [1 ft = 0.3048 m].

this interval. Well AG-99 was drilled in 2011; it encountered Bahariya within 10,256–11,460 ft depth. The maximum thickness of the Lower Cenomanian Bahariya Formation was encountered in this well. Downhole direct pressure measurements indicate an average pore pressure gradient of 0.39–0.42 psi/ft (7.53–8.16 PPG mud weight equivalent), which is slightly less than the hydrostatic gradient. The reservoir interval was drilled with a 10.70 PPG mud weight gradient. The operator had taken out 62 ft of core from the Bahariya Formation (10,720–10,782 ft), selected 63 samples for petrophysical measurements in core lab. Also, direct downhole formation pressure measurements were acquired in the Bahariya reservoir. Wireline logs were gamma ray, deep resistivity, bulk density and neutron porosity.

We used routine core analysis (RCAL) data for the petrophysical characterization of the potential reservoir intervals. RCAL provided grain density, porosity ( $\Phi$ ) acquired by helium porosimeter, and horizontal ( $Kh$ ) and vertical ( $Kv$ ) permeabilities determined by a permeameter. Various lithofacies

were identified from the cores and their hydrocarbon storage and flow capacity were determined from porosity–permeability distribution (Guo et al., 2007; Nabawy et al., 2018; Abuamarah et al., 2019; Baouche et al., 2021b; Abdel-Fattah et al., 2022). Density log was utilized to generate porosity, which was corroborated with core-based measurements. This was useful for estimating porosities in the uncored intervals. To assess the reservoirs’ hydraulic flow properties, we employed the methodology provided by Amaefule et al. (1993), which estimates the reservoir quality index ( $RQI$ ), normalized porosity index ( $NPI$ ), and flow zone indicator ( $FZI$ ) from core-measured porosity and permeability. Pore throat radius ( $R35$ ) was estimated by Windland equation (Winland, 1972; Kolodzie, 1980), thus:

$$\log R35 = 0.732 + 0.588 \log Kh - 0.864 \log \Phi \quad (1)$$

where  $R35$  is in microns. This is a good proxy in the absence of the mercury injection capillary pressure (MICP) test and it works well for both clastics and carbonates (Abuamarah & Nabawy, 2021). Perme-



ability anisotropy ( $\lambda k$ ) was estimated to assess the flow heterogeneity and to infer reservoir pore systems by plotting  $\lambda k$  against various reservoir petrophysical parameters (Serra, 1988), thus:

$$\lambda k = \sqrt{\frac{Kh}{Kv}} \quad (2)$$

We followed the classification proposed by Nabawy et al. (2015) to interpret permeability anisotropy, which defines isotropic to slightly depositional anisotropic fabrics ( $1 < \lambda k < 1.5$ ), moderately depositional anisotropic ( $1.5 < \lambda k < 2.5$ ), highly depositional anisotropic ( $2.5 < \lambda k < 5$ ) and extremely depositional anisotropic fabrics ( $\lambda k > 5$ ). Similarly, secondary anisotropic fabrics were defined by  $\lambda k$  values less than 1 (Nabawy et al., 2015). To define the possible flow, we constructed the stratigraphic modified Lorenz plot (SMLP) (Gunter et al., 1997; Slatt, 2006). We plotted the capacities against depth (El Sharawy & Nabawy, 2016, 2019) and interpreted different hydraulic flow units (HFU). Archie's equation was utilized to estimate water and hydrocarbon saturation (Archie, 1942), while Pickett plot was used to infer the formation water resistivity (Pickett, 1966). The special core analysis (SCAL) was performed only on a few selected samples from the AR-D Member in Well AG-117, which extended the RCAL data to situations more representative of reservoir conditions. The MICP data were recorded in 12 samples, which were used to interpret pore throat size distribution. Water saturation was measured at different applied pressure values (1, 4, 10, 30, 60, 100 and 200 psi<sup>5</sup>) using porous plate method in an oil-brine system. We utilized shale volume  $< 0.35$  and porosity  $> 10\%$  as cutoffs to distinguish potential reservoir flags. In addition, we utilized a water saturation ( $S_w$ ) cutoff of 65% for net pay thickness estimation, as suggested by Rizk et al. (2013) from the AGB Basin. The same  $S_w$  cutoff for net pay was also considered in other Western Desert hydrocarbon fields (Kassab et al., 2019; Abuseda et al., 2021). Relative permeability to oil and water ( $K_{ro}$  and  $K_{rw}$ , respectively) was measured in some samples, and the wettability of various lithofacies was interpreted by plotting these measurements against water saturation (Serra, 1988). The effect of confining pressure on the reservoir porosity and permeability was assessed by measuring porosity and permeability at various

increasing confining pressure (400, 1000, 1500, 2000, 2500, 3300 and 4500 psi).

## RESULTS

### Abu Roash D (AR-D) Member

#### Reservoir Lithofacies

Two potential lithofacies types were identified from the AR-D cores: limestone (LS) and argillaceous limestone (ALS) along with marl (lime mud) intervals (Fig. 3). The LS lithofacies is light to brownish grey, hard, compact, massive and devoid of fossils. Minor stylolites and vertical fractures were observed in the cores. The ALS lithofacies is dark grey in color, argillaceous, with minor pyrite, and occasionally grading into marl. We observed few horizontal fractures within the ALS. The core-measured grain density of the LS lithofacies varied between 2.70 and 2.73 gm/cc with average grain density of 2.70 gm/cc, which is indicative of calcites. The ALS has a grain density range of 2.69–2.73 gm/cc, and the average value was inferred as 2.70 gm/cc (Fig. 3). The bulk density of the LS and ALS ranged 2.38–2.64 gm/cc and 2.63–2.72 gm/cc, respectively.

#### Petrophysical Properties

The RCAL indicates distinct porosity distribution in the two identified lithofacies. The LS lithofacies had a 5–22.4% porosity with average porosity of 12.486%. The ALS lithofacies is very tight with  $< 4\%$  porosity (0.62–4.06%) and average porosity was 1.96% (Fig. 4a). The horizontal permeability of the LS lithofacies varied in the range 0.02–8.42 mD (average 1.225 mD), and the inferred  $\Phi$ – $Kh$  relationship from 60 samples was (Fig. 4a):

$$Kh = 0.00011\Phi^{3.43}, R^2 = 0.72 \quad (3)$$

The tight ALS lithofacies exhibited a  $Kh$  range of 0.003–1 mD<sup>6</sup> (average 0.062 mD) (Fig. 4a). A confident  $\Phi$ – $Kh$  relationship could not be inferred in the argillaceous interval; however, such characteristics may indicate the presence of horizontally connected pores or fractures within the ALS. The vertical permeability of the LS was in the range of 0.019–9.34 mD (average 1.401 mD) while the  $Kv$  in

<sup>5</sup> 1 psi = 0.0069 Megapascal.

<sup>6</sup> 1 mD (millidarcy) = 9.86923\* 10<sup>-16</sup> meter<sup>2</sup>.

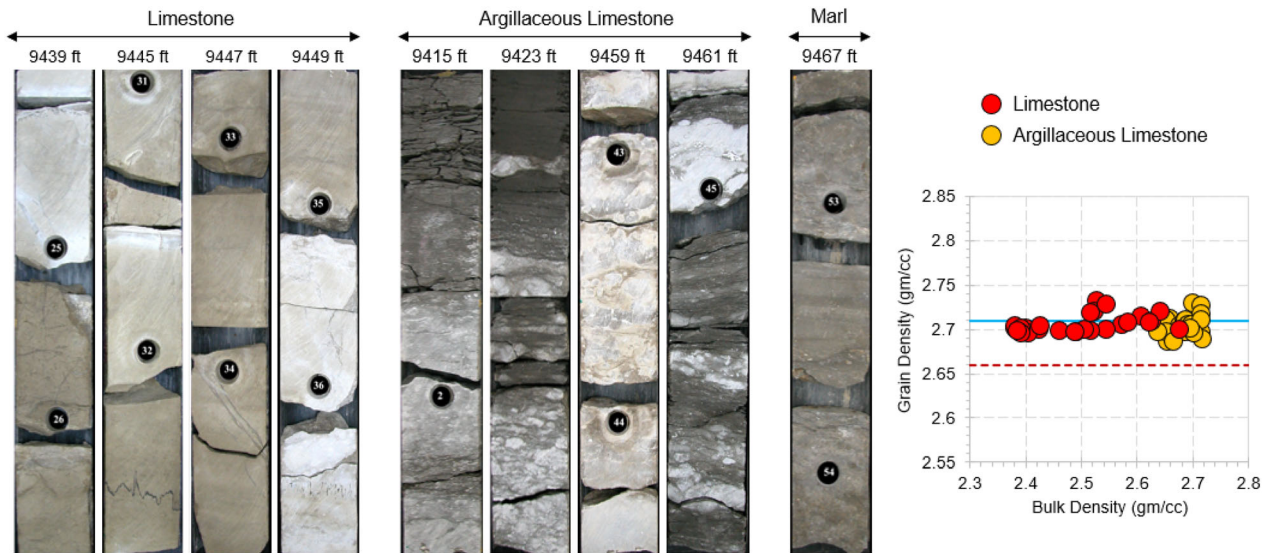


**Figure 3.** Photographs of cores of the two lithofacies types interpreted in the AR-D member and a cross plot of core-measured grain density vs. bulk density. Data belong to Well AG-117. [1 ft = 0.3048 m].

the ALS ranged 0.001–0.028 mD with average of 0.008 mD (Fig. 4b and c). A  $K_v$  cutoff of 0.01 mD distinguished the two lithofacies. The  $K_v:K_h$  of the LS and ALS lithofacies ranged 0.188–5.742 (average 1.96) and 0.06–2.589 (average 0.769), respectively, indicating the presence of both primary depositional fabrics (foliated fabrics) and secondary fabrics (i.e., minor vertically connected pores) (Fig. 4b). The AR-D samples did not exhibit any confident  $K_h$ – $K_v$  correlation. The inferred  $\Phi$ – $K_v$  relationship of the LS lithofacies based on nine data points was (Fig. 4c):

$$K_v = 0.0004\Phi^{3.67}, R^2 = 0.57 \quad (4)$$

Seven  $K_v$  measurements were available from the ALS lithofacies and a confident  $\Phi$ – $K_v$  relationship could not be inferred. The mean hydraulic radius ( $\sqrt{K_h/\Phi}$ ) of the LS and ALS lithofacies ranged 0.615–6.13 mD (average 2.474 mD) and 0.278–4.966 mD (average 1.459 mD), respectively (Fig. 4d). A mean hydraulic radius cutoff of 0.03 mD distinguished the two lithofacies in the AR-D Formation. The mean hydraulic radius was plotted against  $K_v$  (Fig. 4d).

In the stratigraphic modified Lorenz plot (SMLP; Fig. 5), five flow units (HFU 1–5) were identified. The ALS lithofacies consisted of HFU-1 and HFU-5 contributing ~25% of the storage and < 5% of the flow capacity. These were water saturated and characterized by < 4% porosity and average  $K_h$  of 0.062 mD. The LS lithofacies con-

sisted of three flow units (HFU-2, 3 and 4) (Fig. 5). HFU-3 provided the best storage and flow potential characterized by highest porosity (up to 22%) and permeability (up to ~10 mD) being recorded in the AR-D. The HFU-2 and HFU-4 of the LS lithofacies had 7–8% porosity and 0.03–0.5 mD  $K_h$  with high water saturation. The Pickett plot (Fig. 6) indicates formation water resistivity of 0.048  $\Omega$  m and Archie's parameters as  $a = 1$ ,  $m = 2.6$  and  $n = 2$ . Using these parameters, the ALS lithofacies (HFU-1 and HFU-5) as well as the upper and lower intervals of the LS lithofacies (HFU-2 and HFU-4, respectively) were found to be water saturated (Fig. 7). Using a  $S_w$  cutoff of 65%, a 10-ft net pay was identified in the LS lithofacies within 9440–9450 ft, which contributes to the HFU-3. Figure 7 presents the vertical distribution of the interpreted petrophysical properties across the cored interval of the AR-D Member from well AG-117, indicating highest porosity and permeability in the middle part of the studied interval and contributing to the net pay of the LS lithofacies.

#### Special Core Analysis Results

The MICP test indicated that the LS lithofacies had pore throat sizes of 0.1–1.1  $\mu$ m (Fig. 8) which are indicative of micro–mesoporosity. The ALS samples indicated the dominance of nanoporosity (< 0.1  $\mu$ m) (Fig. 9). Capillary pressure data were

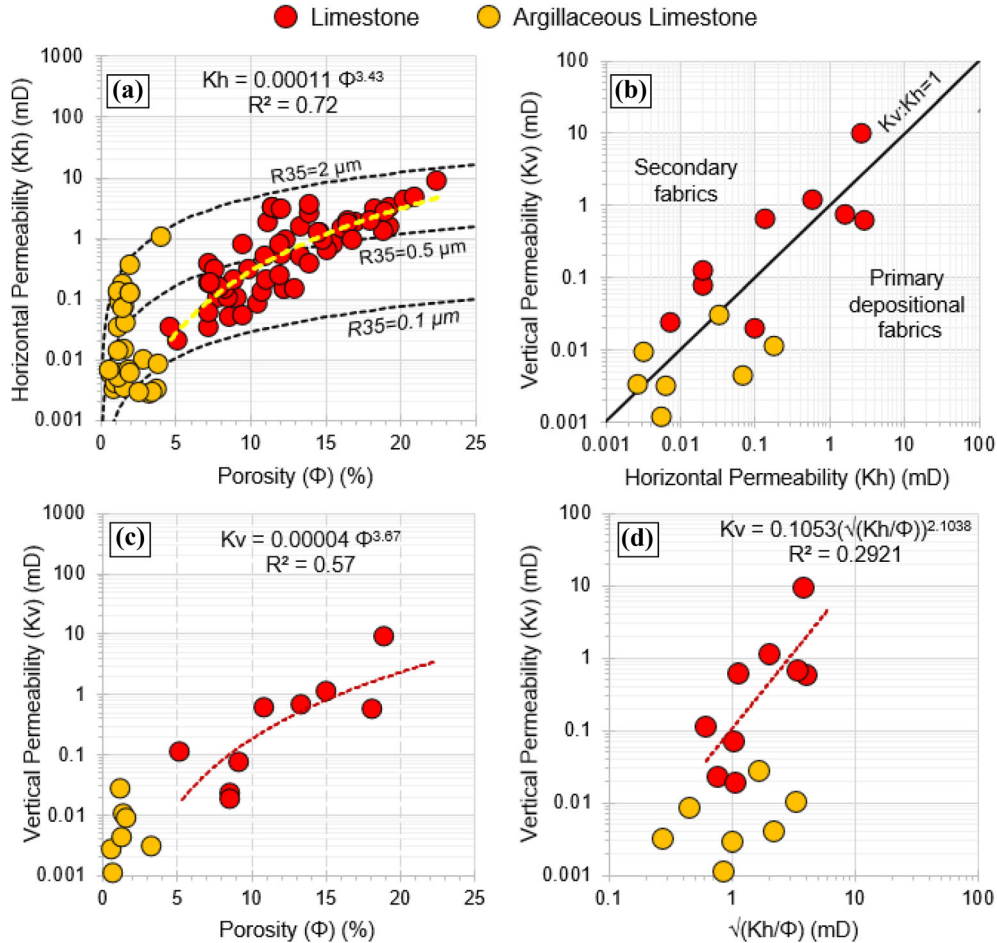


**Figure 4.** Relationships between core-measured (a) porosity ( $\Phi$ ) vs. horizontal permeability ( $K_h$ ); (b) vertical permeability ( $K_v$ ) vs.  $K_h$ ; (c)  $K_v$  vs.  $\Phi$ ; and (d)  $K_v$  vs. mean hydraulic radius ( $\sqrt{K_h/\Phi}$ ), illustrating the porosity–permeability characteristics of both lithofacies types interpreted in the AR-D member. Data belong to Well AG-117. [1 mD (millidarcy) =  $9.86923 \times 10^{-16} \text{ m}^2$ ].

interpreted to infer the fluid saturations in both the lithofacies. The results indicate that the LS lithofacies had lower irreducible water saturation compared to the ALS (Fig. 10; Table 1). Capillary force and wettability may be the controlling factors of elevated irreducible water saturation in the ALS. However, ALS is argillaceous and its higher clay content may also contribute to higher irreducible water saturation. Figure 10 shows very low capillary pressure (< 10 psi) in the LS samples, as the water saturation decreased from 100 to ~ 60%, which implies that 40% of the pore water can be displaced by hydrocarbons at lower pressure condition. Within the ALS lithofacies, water saturation dropped from 100 to ~ 90% as the capillary pressure increased from 1 to 10 psi, implying that only 10% of the free pore water could be displaced in case of the ALS

samples (Fig. 10). The relative permeability vs. water saturation plot (Fig. 11) shows about 31–35% irreducible water saturation in the LS samples and > 50% in the ALS sample, both indicating a strongly water-wet system. The plots of confining pressure vs. porosity and permeability (Fig. 12) indicate that the confining pressure had very slight effect on AR-D rock samples when it increased from 400 to 4500 psi.<sup>7</sup>

*Reservoir Quality and Permeability Anisotropy*

The quality of the AR-D reservoir was characterized by *RQI*, *NPI*, and *FZI* parameters. The *RQI*

<sup>7</sup> 1 psi = 0.0069 Megapascal.

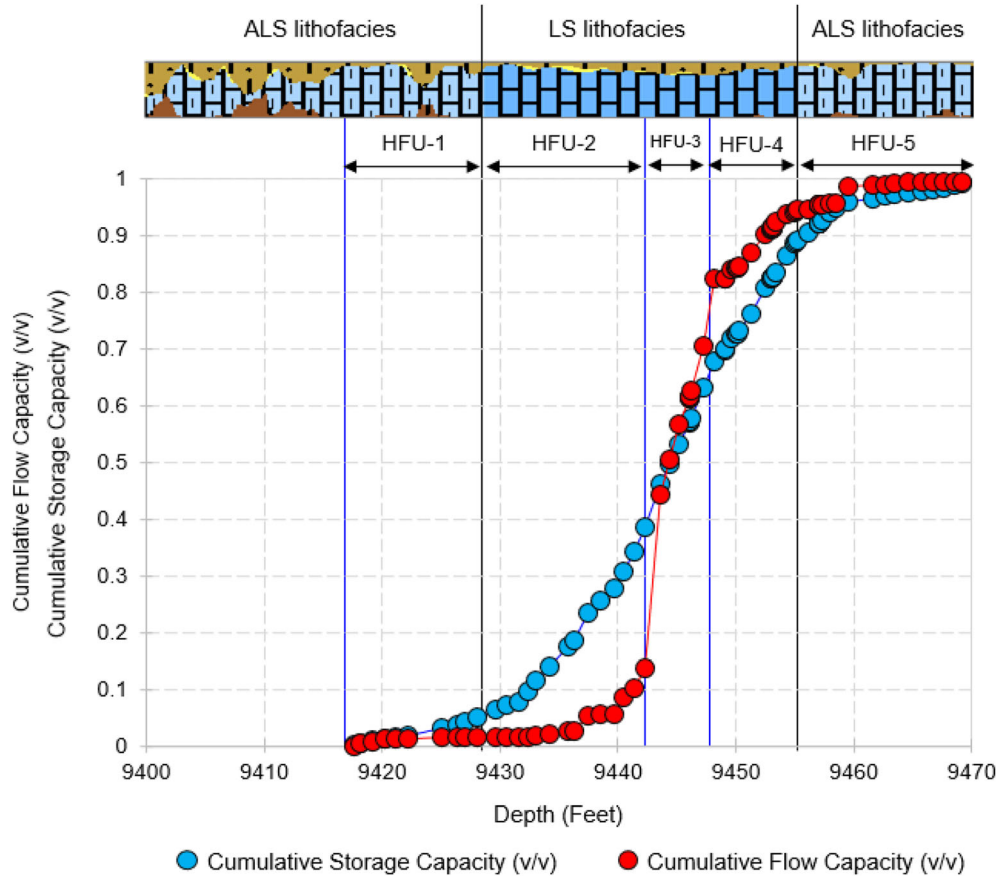


**Figure 5.** Stratigraphic modified Lorenz plots (SMLP) showing flow and storage capacities along with the various hydraulic flow units (HFU) within the AR-D member in Well AG-117.

of both LS and ALS was  $< 0.25 \mu\text{m}$  (Fig. 13a), which is indicative of very poor reservoir quality (i.e., impervious). Due to the very poor permeabilities, the LS lithofacies exhibited  $FZI < 1 \mu\text{m}$  (Fig. 13a). The ALS lithofacies had a wide range of  $FZI$ , the lower end with  $FZI < 2.5 \mu\text{m}$  indicating impervious to poor quality, which is usually expected in a tight formation. However, some data points indicate  $2.5 \mu\text{m} < FZI < 10 \mu\text{m}$ . Such higher  $FZI$  in a tight formation indicates some degree of horizontal pore connectivity. The heterogeneity of hydraulic flow characteristics of the ALS lithofacies is also depicted by Fig. 13b, which shows a  $FZI$  range of  $0.222\text{--}8.491 \mu\text{m}$  against the narrow  $NPI$  range of  $0.049\text{--}0.192$ . Only a few samples of the AR-D were selected for MICP due to the destructive nature of the test. Therefore, we also estimated pore throat sizes from core-based porosity–permeability properties. The LS consisted of micro–mesoporosi-

ties ( $0.137 \mu\text{m} < R35 < 1.457 \mu\text{m}$ ), while the ALS exhibited nano- to mesoporosities ( $0.059 \mu\text{m} < R35 < 1.702 \mu\text{m}$ ) (Fig. 13c–d). The calculated  $R35$  values (from Winland equation) were in good agreement with the MICP data. We inferred that the LS lithofacies represents a poor quality reservoir. The ALS intervals were observed to be tight with poor permeability ( $< 1 \text{mD}$ ) but may have some horizontally connected pores.

Permeability anisotropy ( $\lambda k$ ) of the LS and ALS ranged  $0.417\text{--}2.303$  and  $0.622\text{--}4.098$ , respectively (Fig. 14). Very few of the data points indicate an isotropic pore system and majority of them indicate the presence of secondary pore connectivity. The LS lithofacies was dominated by  $\lambda k < 1$ , indicating secondary anisotropic fabrics, possibly minor vertical fractures (Fig. 14a–c), which yielded high  $K_v:K_h$  ratios. Thin hair line open vertical fractures were also observed in CT scan images of the LS lithofa-



cies (Fig. 15), which strongly support the permeability anisotropy results. In contrast, the ALS lithofacies showed indications of scattered horizontal connected pores resulting in  $\lambda k > 2$  (Fig. 14).

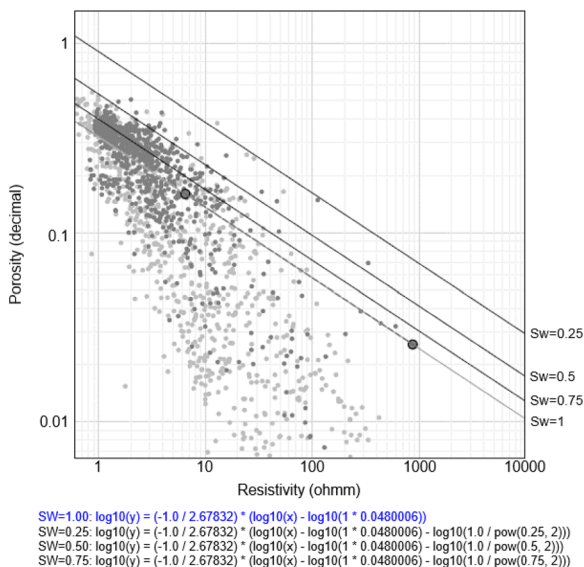


Figure 6. Pickett plot of AR-D member in Well AG-117.

Based on the permeability anisotropy analysis, vertical fractures seem to be negligible in the ALS, which is also characterized by a poor  $K_v$  distribution ( $< 0.03$  mD). The  $RQI-\lambda k$  plot did not show any strong relationship. It is to be noted that  $K_v$  measurements were available from only nine LS samples and seven ALS samples. Majority of the LS samples exhibited the presence of vertical fractures, which offer a wide  $K_v$  range of 0.1–10 mD, while ALS samples exhibited the possible presence of horizontal pore connectivity as well as minor vertical fractures. These heterogeneities, in turn, resulted in difficulties to establish a confident correlation of  $K_v$  with  $K_h$  and porosity. The summary of the petrophysical properties of the LS and ALS lithofacies in the AR-D Member is presented in Table 2.

Abu Roash E (AR-E) Member

Reservoir Lithofacies

Two potential reservoir lithofacies were identified: calcareous sandstone (CS) and glauconitic siltstone (GS) both with intercalated shale intervals. The CS lithofacies is light grey colored, fine- to

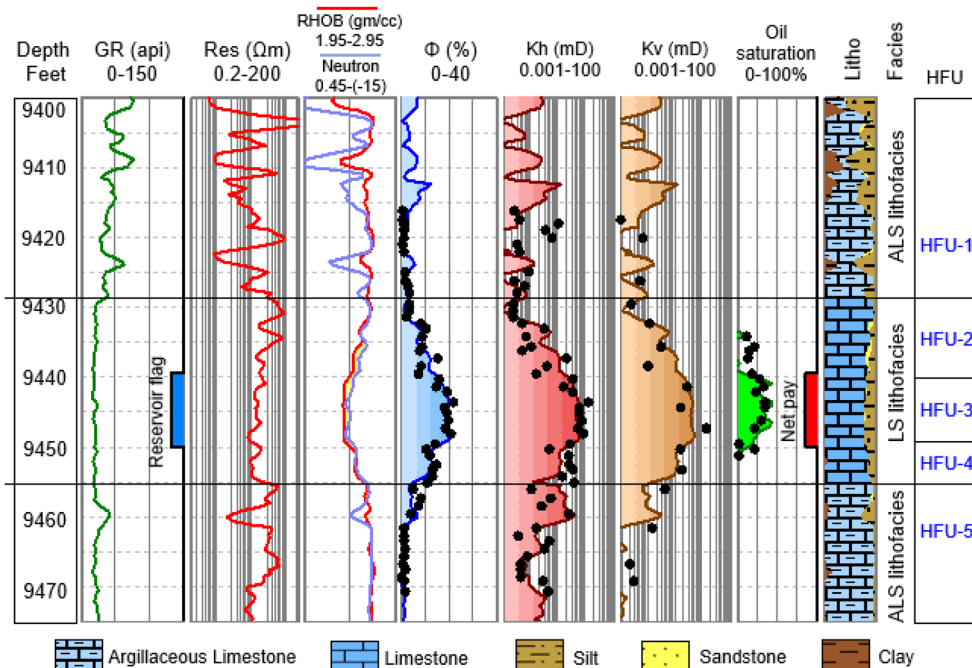
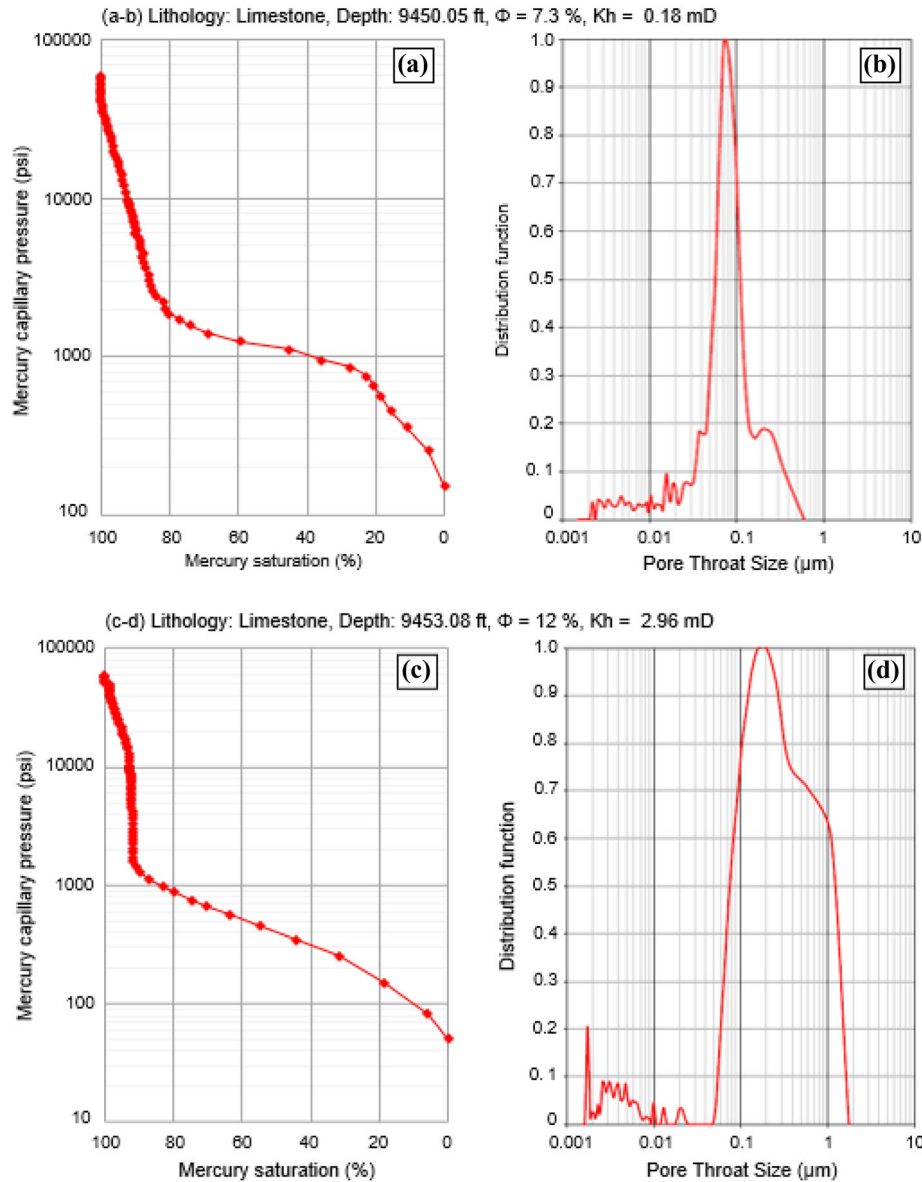


Figure 7. Vertical distribution of lithologic and petrophysical properties within the AR-D member in Well AG-117. Black dots indicate the core measurements. [1 ft = 0.3048 m; 1 mD (millidarcy) =  $9.86923 \times 10^{-16}$  m<sup>2</sup>].





**Figure 8.** Distribution of pore throat size in the limestone lithofacies (LS) of the AR-D member based on the Mercury Injection Capillary Pressure test. Data belong to Well AG-117.

medium-grained, subangular to subrounded, fair to well sorted, moderately hard, and contains calcareous cement. Wavy and flaser beddings are the primary sedimentary structures associated with the CS lithofacies along with minor cross laminations and occasional ferruginous bands (Fig. 16). The GS lithofacies is greenish grey colored, fine to very fine grained, semi-friable, occasionally moderately hard,

and highly glauconite in nature. The cored interval was devoid of fossils. The core-measured grain density of this interval ranged 2.68–2.73 gm/cc, while the average grain densities of the CS and GS were interpreted as 2.68 gm/cc and 2.7 gm/cc, respectively (Fig. 16). The majority of the bulk density data from the CS and GS ranged 2.37–2.47 gm/cc and 2.53–2.63 gm/cc, respectively.

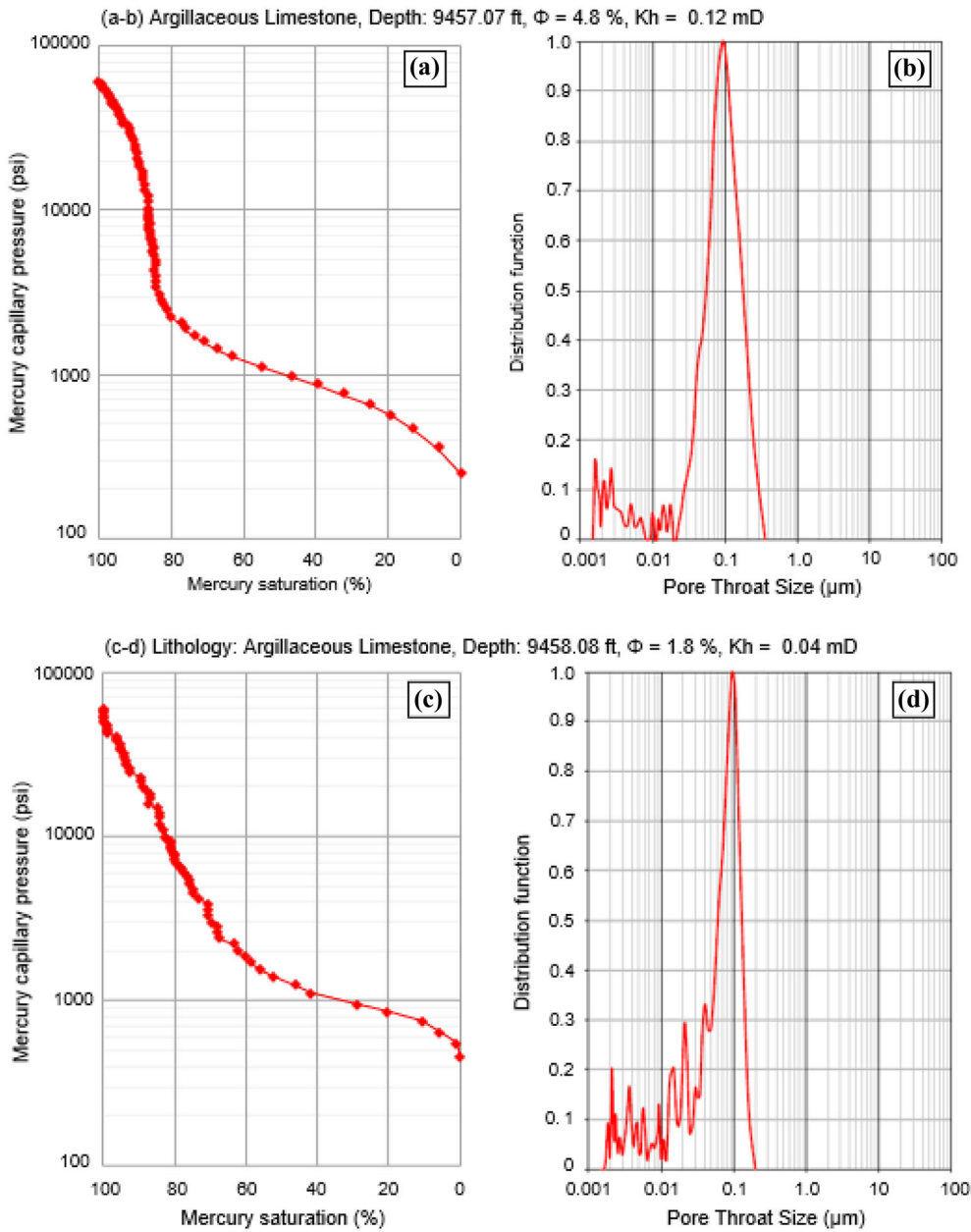


**Figure 9.** Distribution of pore throat size in the argillaceous limestone (ALS) lithofacies of the AR-D member based on the Mercury Injection Capillary Pressure test. Data belong to Well AG-117.

*Petrophysical Properties*

Core measurements indicated a wide range of porosity (3.5–21%) and permeabilities ( $Kh = 0.1$ –305 mD,  $Kv = 0.1$ –168 mD) within the AR-E reservoir. The CS facies were characterized by high porosity (12.9–21%) and horizontal permeability

(9.1–305 mD) compared to the GS facies ( $\Phi = 3.5$ –12.8%,  $Kh = 0.1$ –7.7 mD) (Fig. 17a). The AR-D samples exhibit the following  $\Phi$ – $Kh$  relationship based on 71 samples:

$$Kh = 0.0014\Phi^{3.4019}, \quad R^2 = 0.26 \quad (5)$$

This relationship had a very poor correlation coefficient, but it is clear from Figure 17a that the contribution of porosity to  $Kh$  was more in the CS lithofacies. The  $K_v$  in the AR-E reservoir ranged 0.1–168 mD. The  $K_v/K_h$  ratios ranged 0.1–1.32. The inferred  $K_h$ – $K_v$  relationship from the 71 samples of the AR-E reservoir was:

$$K_v = 0.345K_h^{0.8749}, \quad R^2 = 0.77 \quad (6)$$

Majority of the data distribution indicated  $K_v:K_h \leq 1$ , implying the dominance of primary

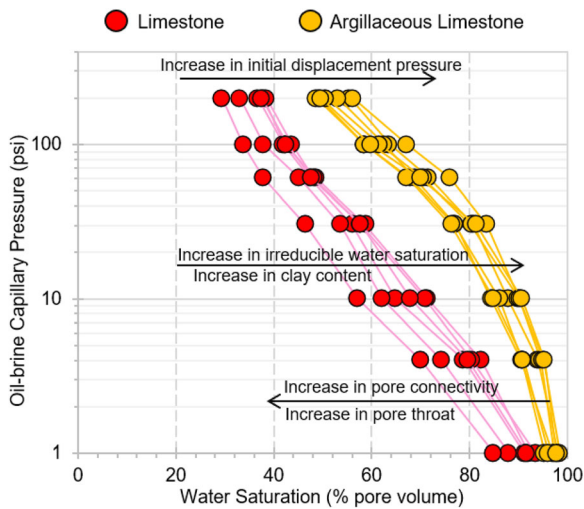


**Figure 10.** Capillary pressure vs. water saturation cross plot using porous plate method in oil–brine system, for both lithofacies types interpreted in the AR-D member. Data belong to Well AG-117. Plot indicates that the argillaceous limestone lithofacies has the higher irreducible water saturation [1 psi = 0.0069 Megapascal].

depositional fabrics in the reservoir lithofacies (Fig. 17b). Some measurements from the GS lithofacies indicated strong permeability difference in horizontal and vertical directions with  $K_h > 1$  mD and  $K_v$  ranging 0.2–0.58 mD (Fig. 17b). The  $\Phi$ – $K_v$  plot (Fig. 17c) could not provide a confident relationship; however, the plot clearly shows two distinct trends within the AR-E reservoir. The CS lithofacies had  $K_v > 1$  mD, while the highest measured  $K_v$  values of the GS facies was 0.58. Very low  $K_v$  values indicate that the pores of the glauconitic siltstone intervals were not at all vertically connected and the porosity did not have much contribution to  $K_v$ . The mean hydraulic radius is plotted against  $K_v$  in Figure 17d, and the following relationship was observed from the 43 samples of CS lithofacies:

$$K_v = 0.0222 \left( \sqrt{K_h/\Phi} \right)^{2.3268}, \quad R^2 = 0.72 \quad (7)$$

The GS lithofacies exhibited very poor relationship between mean hydraulic radius and  $K_v$ . Mean hydraulic radius of the CS (7.426–39.549 mD, average 16.438 mD) was higher than that of the GS lithofacies (1.477–11.547 mD, average 4.005 mD), contributed by higher porosity and horizontal permeability. Based on the data distribution, a porosity cutoff of 15% and permeability cutoffs of  $K_h = 10$  mD and  $K_v = 1$  mD were interpreted in the AR-E reservoir, which differentiate the two lithofacies inferring higher porosity and permeabilities in the CS than in the GS. In the stratigraphic modified Lorenz plot (SMLP; Fig. 18), the GS lithofacies displayed very poor storage and flow capacity and

**Table 1.** Summary of the mercury injection capillary pressure (MICP) measurements showing the variation in capillary characteristics of the LS and ALS lithofacies in the AR-D reservoir, data belongs to the Well AG-117

Capillary pressure (PSI)	Sample no.	Water saturation (% pore volume)						
		1	4	10	30	60	100	200
Limestone lithofacies (LS)	1	91.2	78.9	64.9	56.1	47.3	42	36.7
	2	88	74.3	62.3	53.7	45.2	38	33.2
	3	93.5	80.6	70.9	57.9	48.2	43.7	38.5
	4	92.1	82.5	71.4	58.7	48.7	42.2	38
	5	91.6	79.8	68	57.9	47.7	42.7	37.6
	6	85	70.1	57.2	46.6	38	33.7	29.4
Argillaceous Limestone lithofacies (ALS)	7	96.1	91.1	84.9	76.3	67.4	58.5	48.7
	8	98	94	87.9	80.9	71.8	63.7	55.6
	9	95.4	90.8	86.2	77	67.8	58.6	49.4
	10	97.3	94.5	90.1	83.6	76.1	67.2	56.2
	11	96.9	90.6	84.4	77.2	68.8	62.6	53.2
	12	98.5	95.1	90.2	80.3	70.5	61.6	50.8

marked as HFU-1 and HFU-4. HFU-1 had 4–15% porosity, 0.3–6.2 mD permeability, but the high porosity HFU-1 intervals had higher water saturation (70–85%). HFU-4, identified in the GS lithofacies at the bottom of the studied AR-E Member was found to be water saturated and characterized by lower porosity (< 6%), 0.24–3.5 mD *Kh*. Majority of the flow capacity was provided by the CS lithofacies being distributed in two flow units (HFU-2

and 3) (Fig. 18). These two HFUs had high porosity (~ 20%) and high water saturation (≥ 75%). HFU-3 had slightly higher *Kh* (> 100 mD) than HFU-2 (10–100 mD), which translate to a steeper flow capacity gradient against HFU-3 in the SMLP plot (Fig. 18). Using Pickett plot (Fig. 19), a formation water resistivity was found to be 0.035 Ω m and the Archie’s equation ( $a = 1, m = 1.46, n = 2$ ) provided 52–87% water saturation in AR-E Member. Reservoir flag was interpreted within the CS lithofacies within 10,595–10,618 ft along with the highest porosity–permeability values; however, considering 10% porosity cutoff and 65% *Sw* cutoff, the AR-E did not exhibit any net pay zone. HFU-1 of the GS lithofacies showed < 65% *Sw* within 10,570–10,576 ft but that interval was characterized by < 10% porosity, and so it did not contribute to the net pay (Fig. 20). The vertical distribution of the interpreted petrophysical properties across the cored interval of the AR-E Member from the well AG-37 is presented in Figure 20.

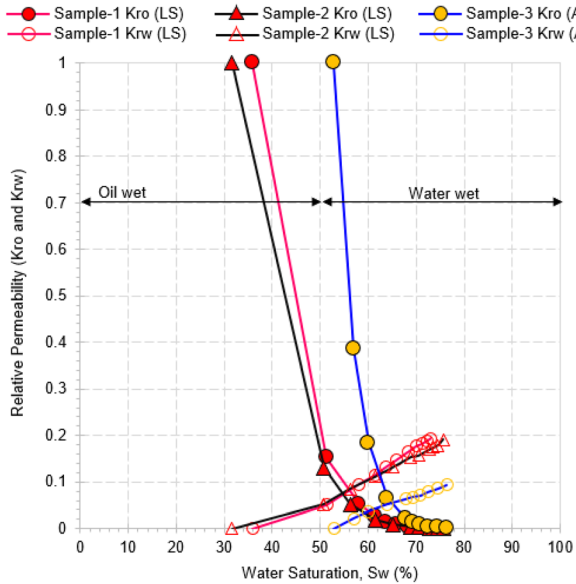


**Figure 11.** Relative permeability of the studied samples from the AR-D member using a water–oil system. ‘*Kro*’ = relative permeability to oil. ‘*Krw*’ = relative permeability to water. ‘LS’ and ‘ALS’ refer to limestone lithofacies and argillaceous limestone lithofacies. Data belong to Well AG-117.

*Reservoir Quality and Permeability Anisotropy*

To characterize the reservoir quality and flow properties, *RQI*, *FZI*, *NPI* and *R35* parameters are plotted for both the lithofacies (Fig. 21). The *RQI* and *FZI* values of the calcareous sandstones range between 0.23–1.24 μm and 1.18–5.12 μm, respectively, which infers a poor to good reservoir quality (Fig. 21a). The GS revealed *RQI* < 0.36 μm and 0.26 μm < *FZI* < 6.1 μm (Fig. 21a). In terms of

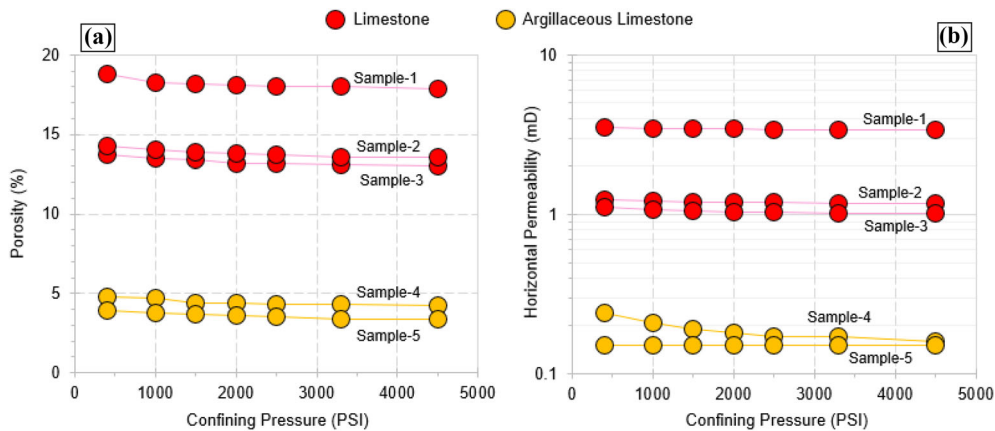


**Figure 12.** Effect of confining pressure on porosity and horizontal permeability of the two lithofacies identified in the AR-D member. Data belong to Well AG-117 [1 psi = 0.0069 Megapascal].

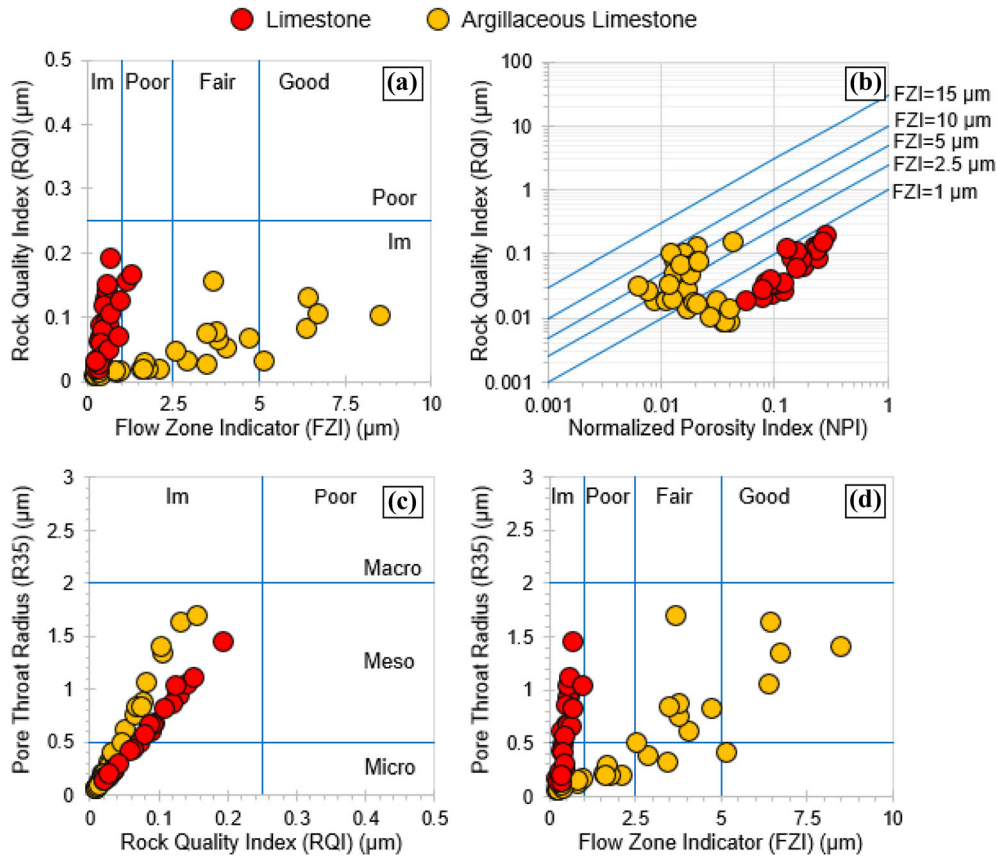


**Figure 13.** Characterization of both lithofacies types interpreted in the AR-D member. Plots of  $RQI$  vs. (a)  $FZI$  and (b)  $NPI$ . Estimated pore throat radius ( $R35$ ) is plotted against (c)  $RQI$  and (d)  $FZI$ . Data belong to Well AG-117. 'Im' indicates 'impervious' quality of the reservoir. Ranks used in (a), (c) and (d) are classified following Nabawy and Al-Azazi (2015).

$RQI$ , the GS lithofacies was mostly impervious (Fig. 21a). The  $NPI-RQI$  cross plot shows that the GS lithofacies primarily has poor hydraulic flow potential, but few measurements indicate higher flow characteristics ( $FZI > 2.5 \mu\text{m}$ ) (Fig. 21a-b) contributed by high  $Kh$ -low  $\Phi$  combination. In absence of MICP measurements, we estimated pore throat size ( $R35$ ) empirically from core-based porosity-permeability properties which revealed a  $R35$  range of 0.35–13.48  $\mu\text{m}$  in the AR-E reservoir (Fig. 21c-d). The CS lithofacies was characterized by  $R35 > 2 \mu\text{m}$  referring to dominantly macroporosity ( $2 \mu\text{m} < R35 < 10 \mu\text{m}$ ) along with some megaporous ( $R35 > 10 \mu\text{m}$ ) spaces while the GS lithofacies was dominantly meso- to microporous ( $0.1 \mu\text{m} < R35 < 0.5 \mu\text{m}$ ) (Fig. 21c-d).

Permeability anisotropy ( $\lambda k$ ) of the AR-E reservoir ranged 0.87–6.20. Both lithofacies dominantly displayed isotropic pore system ( $1 < \lambda k < 2$ ) (Fig. 22a-c) with poor vertical barriers ( $Kh \approx K_v$ ).

However, both lithofacies displayed certain degree of scattered horizontally connected pores (Fig. 22a-c) associated with  $Kh > 2$  mD, which contributed to higher permeability anisotropy ( $\lambda k > 2$ ). We observed that the GS with  $Kh < 1$  mD consisted of only isotropic pores, while the GS intervals with  $Kh$  1–10 mD had scattered horizontal pores. The  $\Phi-\lambda k$  cross plot indicates that the higher porosity lithofacies (i.e., CS) displayed relatively lower  $\lambda k$  when compared to the GS lithofacies characterized by  $\Phi < 15\%$  (Fig. 22c). The  $RQI-\lambda k$  cross plot indicates that the reservoir quality of the CS lithofacies improved from poor to good as permeability anisotropy decreased (Fig. 22d). It is to be noted that both the CS and GS lithofacies of AR-E exhibited the presence of horizontal pore channels and scattered horizontal pores along with the isotropic pore system which yielded a wide  $Kh$  range of 0.1–300 mD. The enhanced horizontal pore connectivity increased  $Kh$  values in both lithofacies, which re-



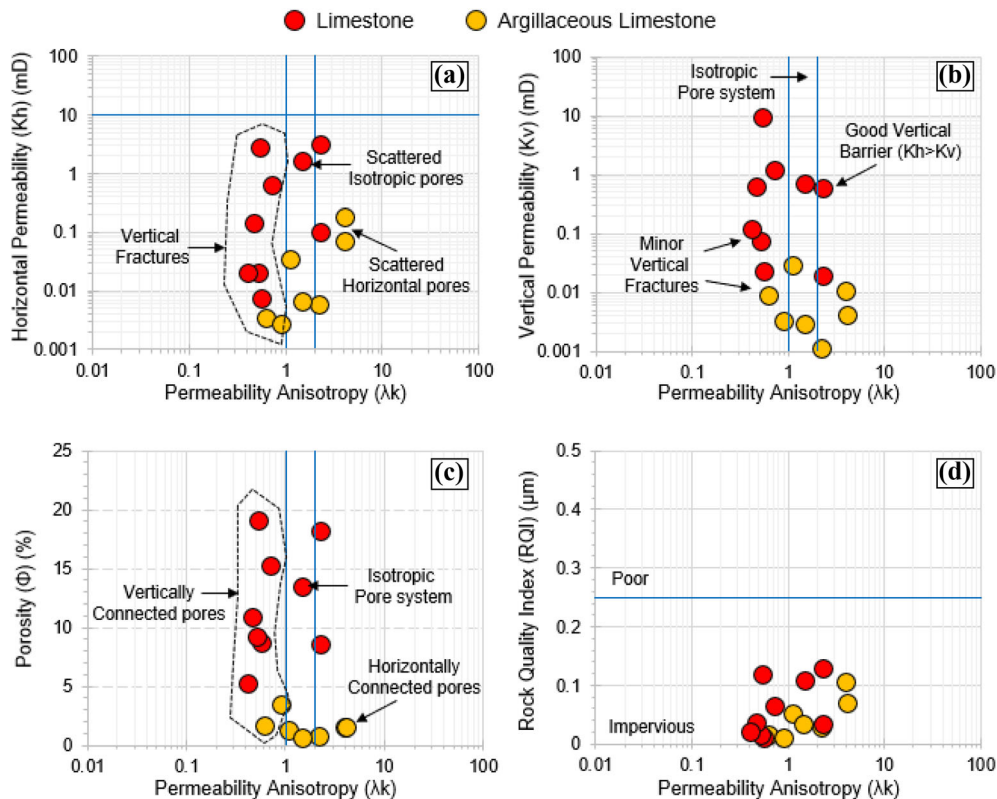


**Figure 14.** Interpretation of flow characteristics of both lithofacies types interpreted in the AR-D member by plotting permeability anisotropy ( $\lambda k$ ) against (a) horizontal permeability ( $K_h$ ), (b) vertical permeability ( $K_v$ ), (c) porosity ( $\Phi$ ) and (d)  $RQI$ . Data belong to Well AG-117. [1 mD (millidarcy) =  $9.86923 \times 10^{-16} \text{ m}^2$ ].

stricted a confident  $\Phi-K_h$  relationship. The summary of the petrophysical properties of the CS and GS lithofacies in the AR-E Member is presented in Table 3.

### Bahariya Formation

#### Reservoir Lithofacies

The reservoir primarily consisted of massive sandstone lithofacies with thin siltstone intercalations (Fig. 23). The sandstones are grey to brownish grey colored, fine to medium grained, moderately cemented, ferruginous, and devoid of fossils. The sandstone unit is mostly massive in nature and contains planar laminations in the lower part. We observed some rounded rip-up clasts within the studied interval. The sandstone commonly grades into siltstone to the top. The siltstone intercalations are light grey colored and exhibit low angle cross stratifications. Thin mud laminae and drapes are also

present. The core-measured grain density of the studied interval ranged 2.63–2.68 gm/cc, while the bulk density exhibits a range of 2.40–2.63 gm/cc (Fig. 23). The majority of the grain density distribution indicates an average of 2.65 gm/cc, which is representative of quartz grains.

#### Petrophysical Properties

Core-based measurements indicated that the Bahariya sandstone reservoir had 8.42–18.4% porosity (average 12.61%) with a  $K_h$  range of 0.58–649.6 mD (average 95.53 mD) (Fig. 24a). The thin siltstone intervals contributed to the lower porosity and permeability ( $\Phi < 10\%$  and  $K_h < 2$  mD). The following  $\Phi-K_h$  relationship was observed in the Bahariya reservoir based on 63 samples:

$$K_h = 0.00000001\Phi^{8.58}, \quad R^2 = 0.84 \quad (8)$$

The vertical permeability ranged 0.2–285 mD (average 58.49 mD) with  $K_v:K_h$  ratios ranging

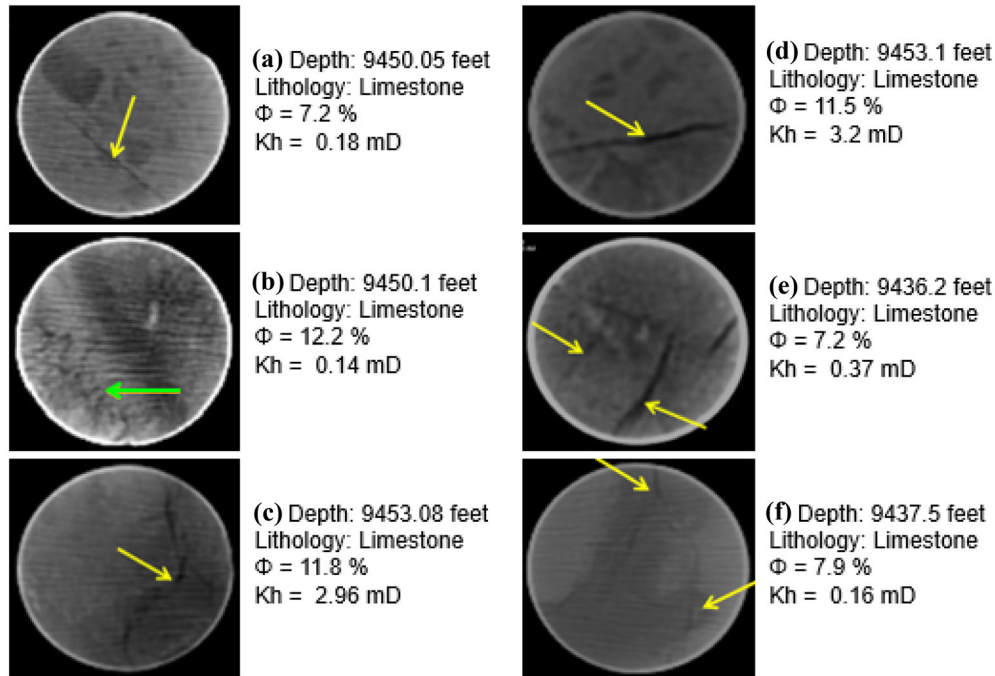


**Figure 15.** CT scan images of core plugs from both lithofacies types interpreted in the AR-D member. Data belong to Well AG-117. Yellow arrows mark hair line vertical fractures along the core plug. Green arrow indicates stylolite. [1 ft = 0.3048 m; 1 mD (millidarcy) =  $9.86923 \times 10^{-16} \text{ m}^2$ ].

**Table 2.** Summary of the core-based petrophysical properties of the AR-D reservoir based on the core measurements.

Petrophysical characteristics	Limestone lithofacies (LS)				Argillaceous limestone lithofacies (ALS)			
	Min	Max	Avg	CV	Min	Max	Avg	CV
Porosity ( $\Phi$ ) (%)	4.7	22.406	12.486	0.339	0.62	4.06	1.96	0.506
Horizontal Permeability ( $K_h$ ) (mD)	0.02	8.42	1.225	1.258	0.003	1	0.062	2.374
Vertical Permeability ( $K_v$ ) (mD)	0.019	9.34	1.401	2.144	0.001	0.028	0.008	1.105
$K_v/K_h$	0.188	5.742	1.96	1.076	0.06	2.589	0.769	1.178
Permeability Anisotropy ( $\lambda_k$ )	0.417	2.303	1.211	0.611	0.622	4.098	2.073	0.705
Mean Hydraulic Radius (mD)	0.615	6.130	2.474	0.580	0.278	4.966	1.459	0.879
Grain Density (gm/cc)	2.695	2.732	2.705	0.004	2.686	2.73	2.703	0.004
Rock Quality Index ( $RQI$ ) ( $\mu\text{m}$ )	0.019	0.192	0.078	0.579	0.009	0.156	0.046	0.879
Normalized Porosity Index ( $NPI$ )	0.049	0.289	0.145	0.389	0.006	0.042	0.02	0.518
Flow Zone Indicator ( $FZI$ ) ( $\mu\text{m}$ )	0.218	1.275	0.534	0.481	0.222	8.491	2.823	0.809
Pore Throat Radius ( $R_{35}$ ) ( $\mu\text{m}$ )	0.137	1.457	0.584	0.637	0.059	1.702	0.526	0.96

'Avg' and 'CV' refer to the average values and coefficient of variation [1 mD (millidarcy) =  $0.986923 \times 10^{-15} \text{ meter}^2$ ]

0.11–0.96 (average 0.528). Thus, the Bahariya reservoir exhibited a poor  $K_v$ – $K_h$  relationship ( $R^2 < 0.5$ ) (Fig. 24b). Majority of the measurements indicated  $K_v:K_h$  of  $> 0.5$ . The  $K_v:K_h < 1$  in the Bahariya reservoir indicates the presence of primary depositional fabrics (Fig. 24b). The  $\Phi$ – $K_v$  plot (Fig. 24c) provided the following relationship based on 22 measurements:

$$K_v = 0.00000001\Phi^{8.34}, \quad R^2 = 0.76 \quad (9)$$

The mean hydraulic radius ranged 2.602–59.413 mD (average 19.466 mD) and it exhibited poor relationship with  $K_v$ .

In the stratigraphic modified Lorenz plot (SMLP; Fig. 25), five flow units (HFU-1 to HFU-5) were identified within the cored Bahariya reservoir

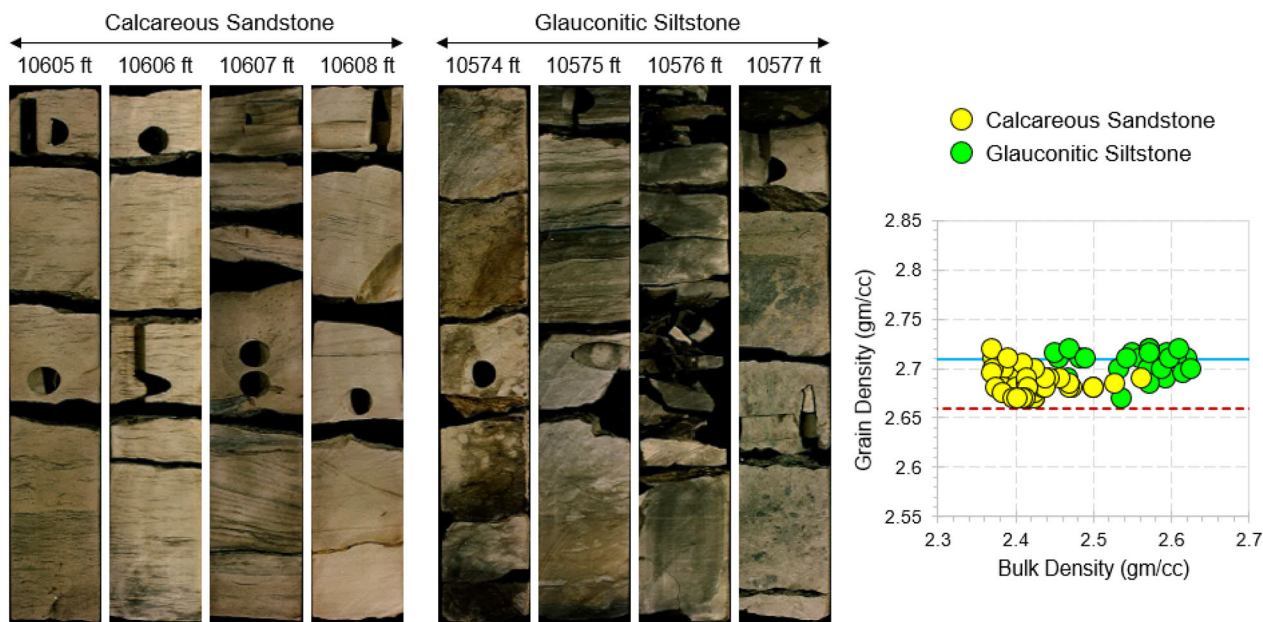


Figure 16. Photographs of cores of the two lithofacies types interpreted in the AR-E member and a cross plot between core-measured grain density vs. bulk density. Data belong to Well AG-37 [1 ft = 0.3048 m].

interval. Breaks in slope of the SMLP indicated the presence of flow baffles within the Bahariya reservoir, indicating heterogeneity. HFU-1, 3 and 5 had similar porosity ranges (8–12%) and < 100 mD Kh. HFU-2 and HFU-4 were characterized by relatively higher porosity (12–18%) and Kh of > 100 mD, which yielded steeper flow capacity gradients against these two units in the SMLP plot (Fig. 25). Using Pickett plot (Fig. 26), a formation water resistivity was found to be 0.03 Ω.m and the Archie’s equation ( $a = 1$ ,  $m = 1.84$ ,  $n = 2$ ) provided 70–80% water saturation in the lower part of the Bahariya Formation, where core measurements were available. Therefore, all the HFUs were highly water saturated. Reservoir flags were interpreted in the CS lithofacies within 10,595–10,618 ft along based on cutoffs of > 10% porosity and < 0.35 shale volume. However, the cored interval of the Bahariya exhibited  $S_w > 65\%$  and therefore devoid of any net pay zone. Based on the log-based estimates, net pay was recognized within 10,663–10,713 ft, which lies above the cored interval (Fig. 27). The vertical distribution of porosity and permeabilities across the cored interval of the Bahariya Formation from the well AG-99 is presented in Figure 27.

Reservoir Quality and Permeability Anisotropy

The quality of the Bahariya reservoir was deciphered by RQI, NPI and FZI estimated from the core-based porosity–permeability measurements. The RQI and FZI ranged 0.08–1.87 μm and 0.88–8.91 μm, respectively (Fig. 28a). These broad ranges of RQI and FZI indicate poor to good reservoir qualities in the sandstone intervals ( $2.5 \mu\text{m} < FZI < 10 \mu\text{m}$ ) while the thin siltstone intercalations appeared to be impervious to poor quality ( $RQI < 0.25 \mu\text{m}$  and  $FZI < 2.5 \mu\text{m}$ ). In the absence of MICP measurements, we estimated pore throat size (R35) empirically from core-based porosity–permeability properties, which revealed a R35 range of 0.67–22.06 μm in the Bahariya reservoir (Fig. 28d). The sandstone intervals indicated macro- and megaporosity while the intercalated siltstones were microporous ( $0.5 \mu\text{m} < R35 < 2 \mu\text{m}$ ).

Permeability anisotropy ( $\lambda k$ ) of the Bahariya reservoir ranged 1.02–3.02. The majority of the data distribution was indicative of isotropic pore system ( $1 < \lambda k < 2$ ) (Fig. 29a–c), which is contributed by the primary depositional fabrics. Only three mea-

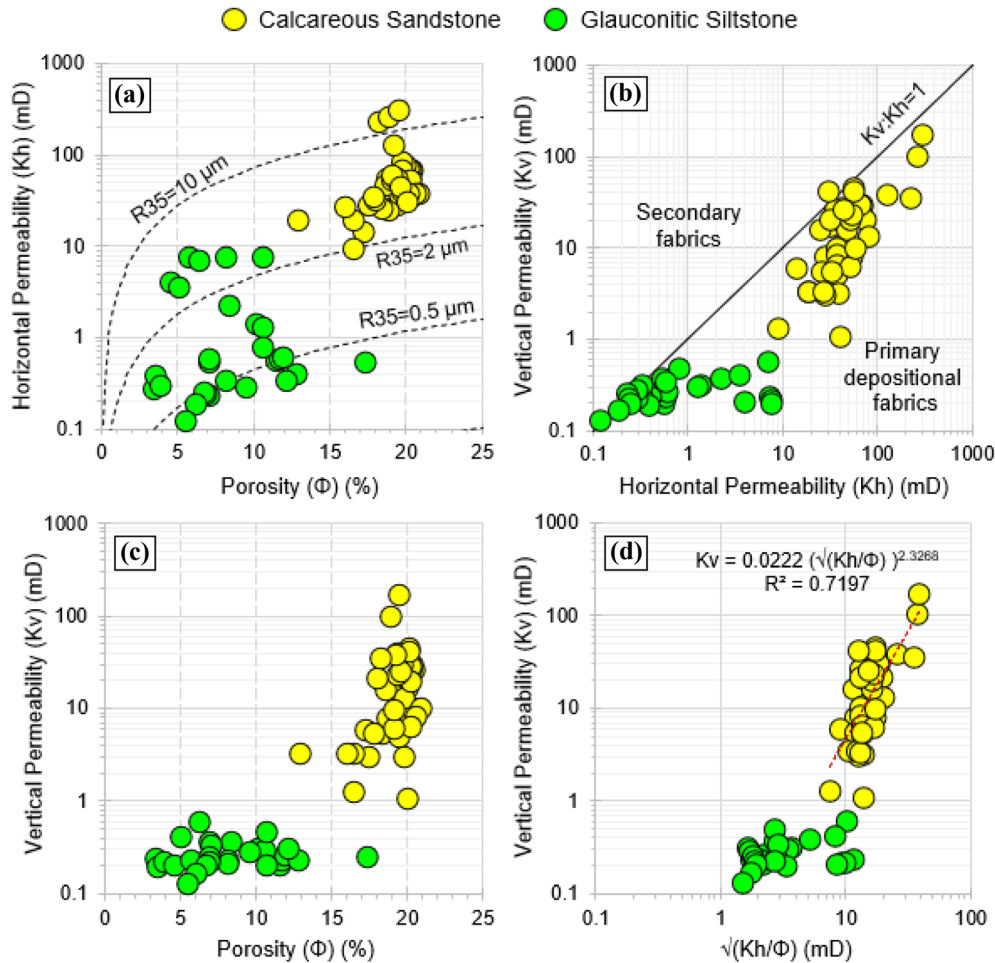


**Figure 17.** Relationships between core-measured (a) porosity ( $\Phi$ ) vs. horizontal permeability ( $K_h$ ); (b) vertical permeability ( $K_v$ ) vs.  $K_h$ ; (c)  $K_v$  vs.  $\Phi$ ; and (d)  $K_v$  vs. mean hydraulic radius ( $\sqrt{K_h/\Phi}$ ), illustrating the porosity–permeability characteristics of both lithofacies types interpreted in the AR-E member. Data belong to Well AG-37 [1 mD (millidarcy) =  $9.86923 \times 10^{-16} \text{ m}^2$ ].

measurements displayed  $\lambda k > 2.5$  (2.77–3.02), indicating very minor influence by horizontal pore connectivity (Fig. 29a–c). The homogenous distribution of the pore characteristics was also reflected by the  $RQI$ – $\lambda k$  cross plot (Fig. 29d). The summary of the petrophysical properties of the CS and GS lithofacies in the AR-E Member is presented in Table 4.

## DISCUSSIONS

### AR-D Reservoir

Based on the presence of carbonate-dominated sequences within the AR-D Member, Sarhan et al. (2017a, 2017b) interpreted a marine environment in the nearby Gindi Basin. Ghassal et al. (2018) ana-

lyzed the organic geochemistry of oil-stained AR-D core samples from the GPT field in the AGB and inferred a shallow marine environment due to the presence of a mixed marine and terrestrial palynofacies. Overall, the LS and ALS lithofacies of the AR-D Member refers to a calm and low energy depositional environment in a shallow marine shelf setting (Burchette & Wright, 1992), which prevailed during the Turonian (Mansour et al., 2020). In the studied reservoir interval, the ALS lithofacies lies above and below the LS. The MICP test indicated micro–mesoporosity in the LS while the ALS was nanoporous (Figs. 7 and 8) and tight (< 4% porosity) due to its higher clay content, which closed the pore throats. The ductility of the clay matrix was also responsible for the poor preservation potential of porosity–permeability under increasing confining



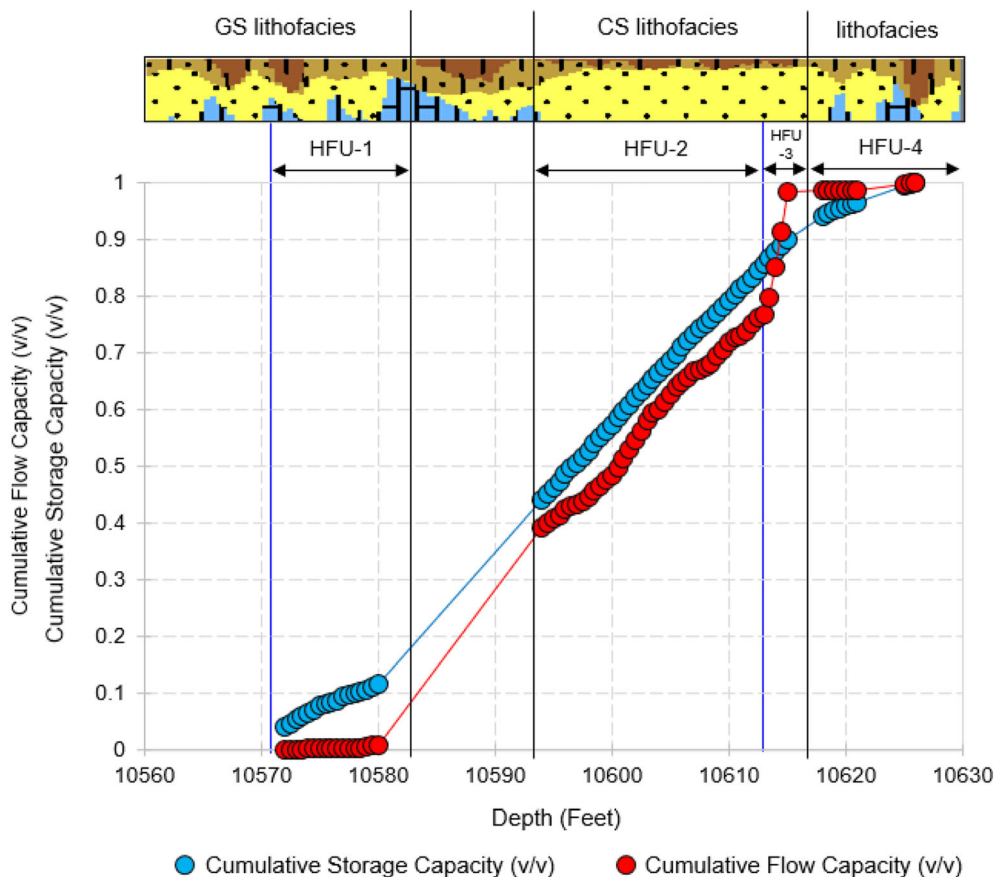


**Figure 18.** Stratigraphic modified Lorenz plots (SMLP) showing flow and storage capacities along with the various hydraulic flow units (HFU) within the AR-E member in Well AG-37.

stress. The average  $K_v:K_h < 1$  in the ALS indicated that the primary depositional fabrics were dominantly preserved; however, some degrees of horizontal pore connectivity enhanced the anisotropy and thus provided a good vertical permeability barrier.

The LS lithofacies is massive in nature and devoid of fossils and we did not observe dissolution features. However, compaction was observed to be the main post-depositional diagenetic modification within the studied lithofacies. We observed rectangular or columnar stylolites within the LS (Fig. 3), which indicates the presence of chemical compaction at the later stage of diagenesis. Stylolites are secondary (chemical) sedimentary structures formed by pressure dissolutions as a result of overburden pressure (Koehn et al., 2016). Stylolites can have wide ranging effects on the porosity and permeability of host rocks. The common opinion is that

they reduce the flow potential and act as permeability barriers (Alsharhan & Sadd, 2000; Baud et al., 2012; Heap et al., 2014). However, many researchers reported porosity enhancement associated with stylolite formation (Gingras et al., 2002; Harris, 2006). Lind et al. (1994) could not find any distinguishing effect of stylolites on the flow potential of high porosity chalk reservoirs. The stylolitic intervals of the LS lithofacies (9445 ft, 9449 ft) are associated with high porosity (14.68–19.27%) and poor permeability ( $K_h = 1.24\text{--}3.22$  mD), which indicate that the stylolites may have a negative impact in reservoir flow capacity. However, complimentary laboratory data to infer its detailed impact on the AR-D reservoir quality were unavailable in this study. We also observed minor fractures within the AR-D cores. Fractures are indicative of mechanical compaction (Barbier et al., 2012). The LS lithofacies exhibited lower permeability aniso-



trophy values (mostly < 1 mD), which indicate the influence of some minor vertical fractures.

Overall, the studied AR-D interval is nano- to mesoporous and the reservoir quality is inferred as impervious to poor with dominantly < 1 mD per-

meability in spite of the presence of vertical fractures. The petrophysical cutoffs indicated a 10-ft pay zone within the LS lithofacies. A stimulation strategy is absolutely necessary to produce from these carbonates. Following the tight carbonate field development examples worldwide, specially middle east and Egypt (Salamy et al., 2006; Al-Hajeri et al., 2007; George et al., 2012; Chimmalgi et al., 2013; Alyan et al., 2015; Sen et al., 2021), we recommend that coil tubing (CT) carried gun and acid stimulation will be helpful to activate this tight reservoir. Latief et al. (2019) discussed the results and utility of underbalanced drilling strategy to enhance production from a carbonate reservoir with 10–18% porosity and 0.2–1.5 mD permeability, very similar to the studied AR-D interval. Authors reported threefold oil production increase as the bottomhole pressure was reduced by 20% below formation pressure during underbalanced drilling with nitrogen injection (Latief et al., 2019). A similar strategy has yet not been tested in any Egyptian carbonate reservoir but it is worth considering. A horizontal well bore would have been the ideal strategy to achieve maximum reservoir contact; however, this might not be the best suitable considering the availability of multiple reservoir units within a single

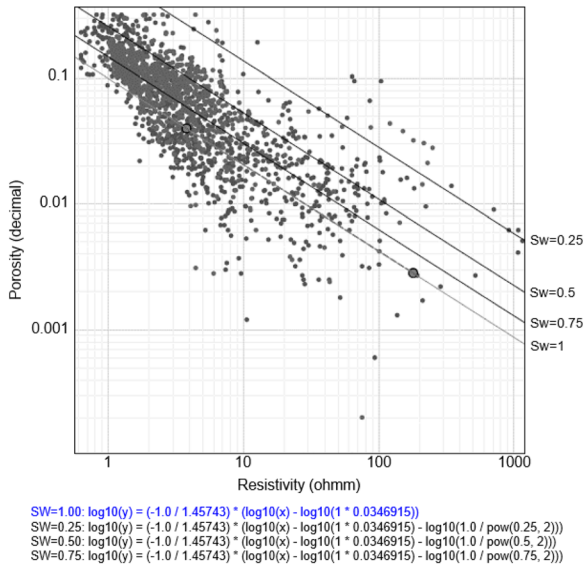


Figure 19. Pickett plot of AR-E member in Well AG-37.

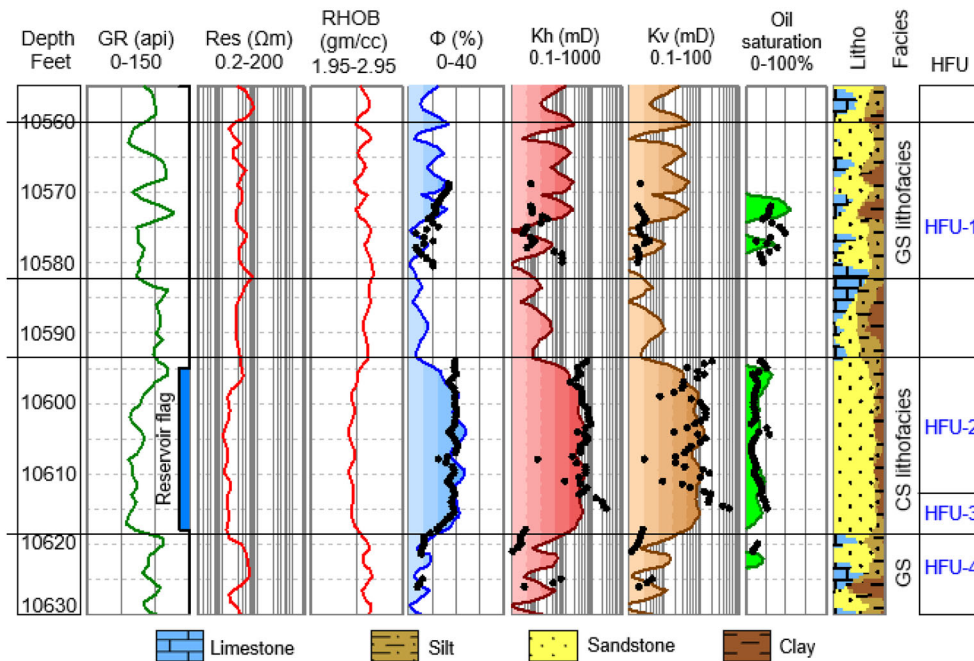
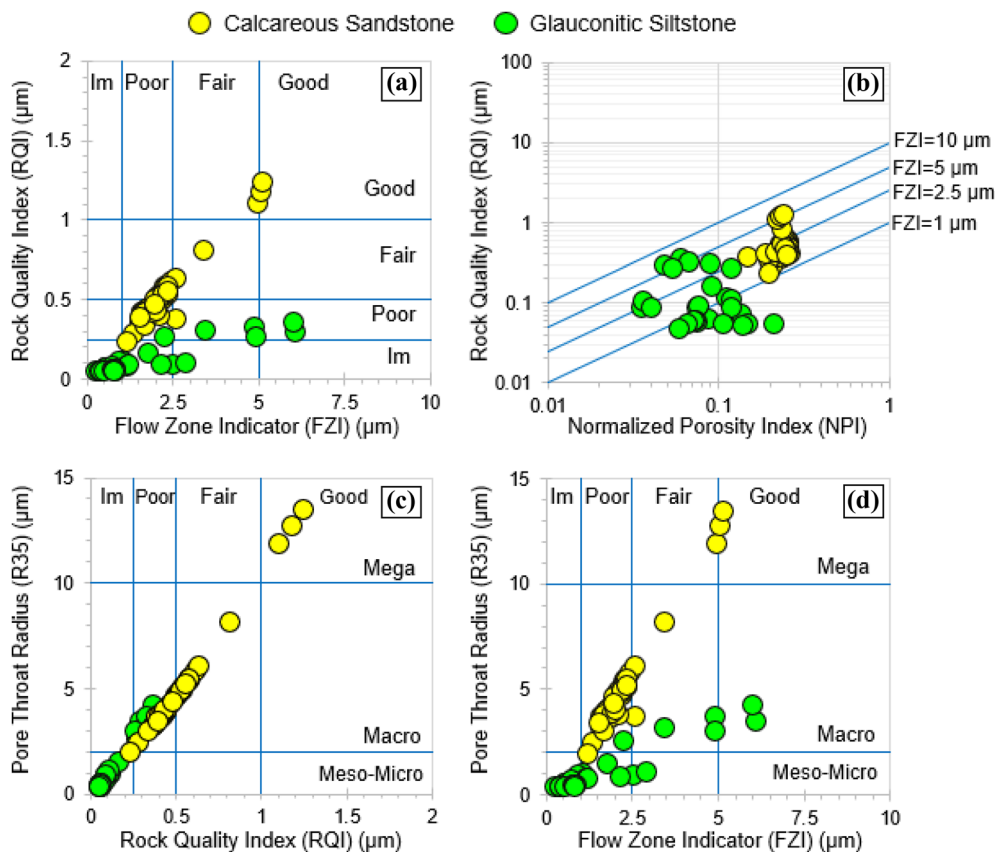


Figure 20. Vertical distribution of lithologic and petrophysical properties within the AR-E member in the Well AG-37. Black dots indicate the core measurements. [1 ft = 0.3048 m; 1 mD (millidarcy) = 9.86923 × 10<sup>-16</sup> m<sup>2</sup>].



**Figure 21.** Characterization of both lithofacies types interpreted in the AR-E member. Plots of *RQI* vs. (a) *FZI* and (b) *NPI*. Estimated pore throat radius (*R35*) is plotted against (c) *RQI* and (d) *FZI*. Data belong to Well AG-117. ‘Im’ indicates ‘impervious’ quality of the reservoir. Ranks used in (a), (c) and (d) are classified following Nabawy and Al-Azazi (2015).

well (AR-D, E, G and Bahariya reservoirs). Multi-lateral wells or stacked multibranch wells can be more suitable for such scenario if the cost implications work out favorably. In March 2013, another well (AG-108) was drilled to test the AR-D reservoir, but it did not flow naturally. Therefore, acid stimulation was conducted, and it showed oil and gas production rates of 2600 BOPD<sup>8</sup> (barrel oil per day) and 6 MMSCFD<sup>9</sup> (million standard cubic ft/day), respectively (Khalda Petroleum Company, 2013). However, the AR-D reservoir is strongly water wet with high irreducible water saturation (> 30% in the LS and ~ 50% in the ALS lithofacies) and it will critically affect the producible hydrocarbon volume.

<sup>8</sup> 1 bopd = 0.1589 cubic meter per day.

<sup>9</sup> 1 MMSCFD (million standard cubic ft/day) = 0.02832 MMSCMD (million standard cubic meter/day).

### AR-E Reservoir

The studied upper AR-E interval was composed of CS and GS, and it exhibited a fining upward trend. This section was devoid of any limestone bed. The occurrence of wavy-flaser beddings and cross laminations within the CS lithofacies indicated a relative moderate energy condition in a subtidal depositional environment, i.e., a tidal channel. The sharp change in the gamma ray log value at the base of the LS lithofacies (~ 10,620 ft in Fig. 20) marked the base of the tidal channel complex. We had observed few ferruginous bands within the CS, which may suggest sub-aerial exposure that is common in tidal settings (Hewaidy et al., 2018). The association of GS lithofacies was critical to infer the depositional environment. Glauconite occurrences are reported from a wide range of environments, i.e.,

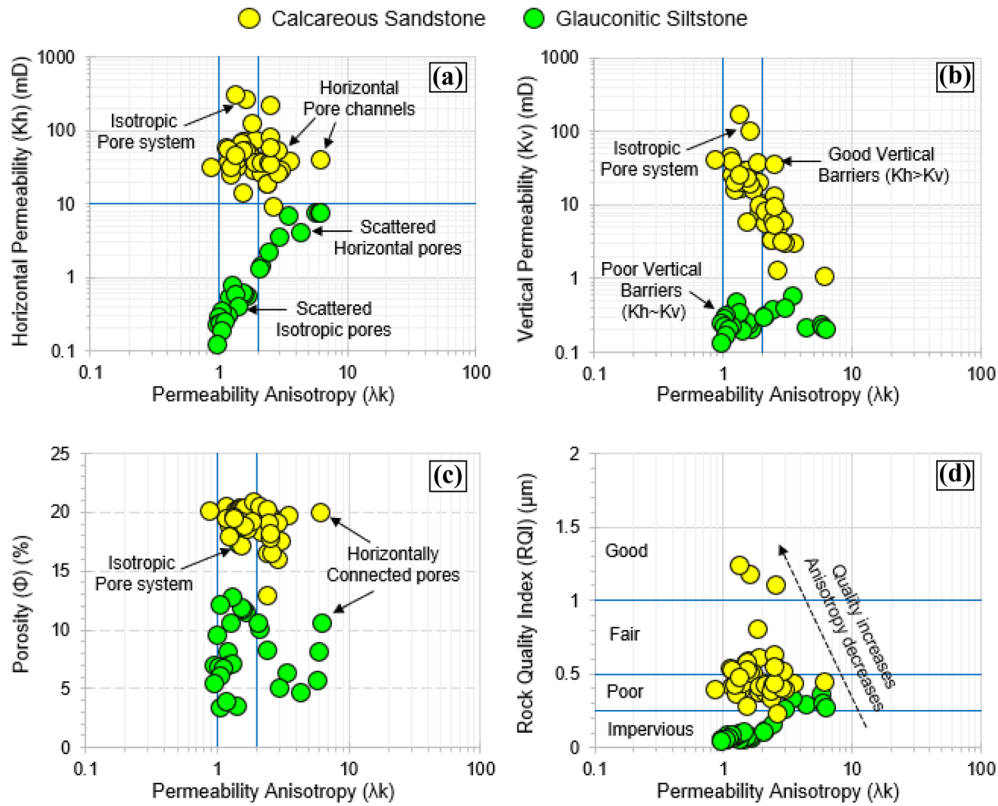


**Figure 22.** Interpretation of flow characteristics of both lithofacies types interpreted in the AR-E member by plotting permeability anisotropy ( $\lambda k$ ) with (a) horizontal permeability ( $K_h$ ), (b) vertical permeability ( $K_v$ ), (c) porosity ( $\Phi$ ) and (d)  $RQI$ . Data belong to Well AG-37 [1 mD (millidarcy) =  $9.86923 \times 10^{-16}$  meter<sup>2</sup>].

**Table 3.** Summary of the core-based petrophysical properties of the AR-E reservoir based on the core measurements.

Petrophysical characteristics	Calcareous sandstone lithofacies (CS)				Glauconitic siltstone lithofacies (GS)			
	Min	Max	Avg	CV	Min	Max	Avg	CV
Porosity ( $\Phi$ ) (%)	12.9	20.9	19.088	0.079	3.4	17.3	8.284	0.398
Horizontal Permeability ( $K_h$ ) (mD)	9.1	305	60.199	1.013	0.12	7.7	1.782	1.429
Vertical Permeability ( $K_v$ ) (mD)	1.06	168	22.318	1.293	0.13	0.58	0.272	0.357
$K_v/K_h$	0.026	1.322	0.362	0.688	0.259	1.087	0.519	0.673
Permeability Anisotropy ( $\lambda k$ )	0.869	6.143	2.016	0.445	0.959	6.204	2.101	0.756
Mean Hydraulic Radius (mD)	7.426	39.549	16.438	0.404	1.477	11.547	4.005	0.786
Grain Density (gm/cc)	2.67	2.72	2.685	0.004	2.67	2.72	2.705	0.005
Rock Quality Index ( $RQI$ ) ( $\mu m$ )	0.233	1.242	0.516	0.404	0.046	0.363	0.126	0.785
Normalized Porosity Index ( $NPI$ )	0.148	0.264	0.236	0.948	0.351	0.209	0.091	0.439
Flow Zone Indicator ( $FZI$ ) ( $\mu m$ )	1.18	5.127	2.189	0.404	0.263	6.068	1.779	0.979
Pore Throat Radius ( $R_{35}$ ) ( $\mu m$ )	1.962	13.483	4.891	0.495	0.355	4.237	1.229	0.963

‘Avg’ and ‘CV’ refer to the average values and coefficient of variation [1 mD (millidarcy) =  $0.986923 \times 10^{-15}$  meter<sup>2</sup>]

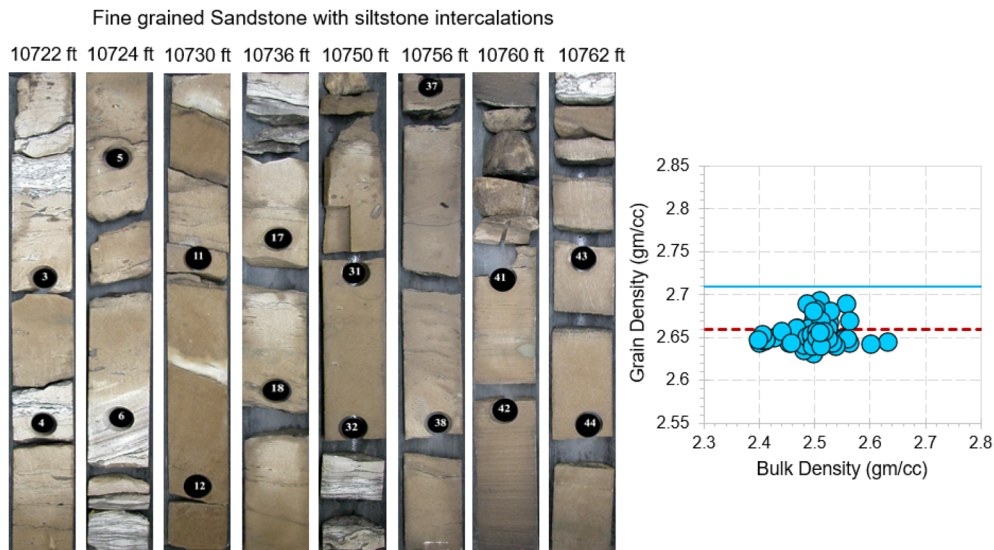


**Figure 23.** Photographs of cores of the Bahariya Formation and a cross plot between core-measured grain density vs. bulk density. Data belong to Well AG-99 [1 ft = 0.3048 m].

shallow marine shelf, slope, deep marine, lacustrine, tidal, estuarine, lagoon, deltaic to fluvio-deltaic etc. (Banerjee et al., 2016a; Bansal et al., 2018). Farouk (2015) reported a shallow subtidal environment for the glauconitic sandstones of the Cenomanian Galala Formation from Egypt. Very low sedimentation rate and poor terrigenous clastic influx associated with a rapid sea-level rise in the warm climatic condition provides the ideal condition and required shallow substrates for extensive glauconitization (Banerjee et al., 2015; 2016a, b; 2019; Bansal et al., 2019). The GS of the AR-E are associated with the shale intervals (high gamma ray values in Fig. 20), which may indicate that these glauconites are autochthonous (Baoumy & Boulis, 2012). The lithological description available from the core report indicated that the shales associated with the reservoir interval (~ 10,585–10,595 ft in Fig. 20) contained carbonaceous material, possibly indicating tidal flat deposits. Based on the facies association, we concluded that the studied AR-E interval was deposited in a tidal depositional environment in transgressive system. A few researchers reported fresh water algae in the lower part of the AR-E,

which is indicative of increased influx terrestrial organic matter possibly influenced by a drop in sea level (Abdel-Kireem et al., 1996; Zobaa et al., 2011). However, our studied interval belongs to the upper part of the AR-E Member. Boukhary et al (2014) deciphered that a shallow marine to open marine environment prevailed in the eastern AGB during the Turonian and deposited the AR-F to AR-A Members, which correlates well with our observations.

Both lithofacies preserve primary depositional fabrics (Fig. 17b) and consist of isotropic pore system along with some connected horizontal pores (Fig. 22) yielding higher permeability anisotropy. However, the two lithofacies exhibit distinct storage and flow characteristics. The CS facies was generally macroporous with some megaposity and possessed excellent porosity (> 15%) and permeability (~ 10–305 mD) aided by a higher mean hydraulic radius of > 1 mD. The mesoporous GS lithofacies was characterized by poor porosity–permeability behavior due to the presence of fine glauconites (which had a general size range of 60–1000 μm). We concluded that the tidal channel facies of the AR-E had

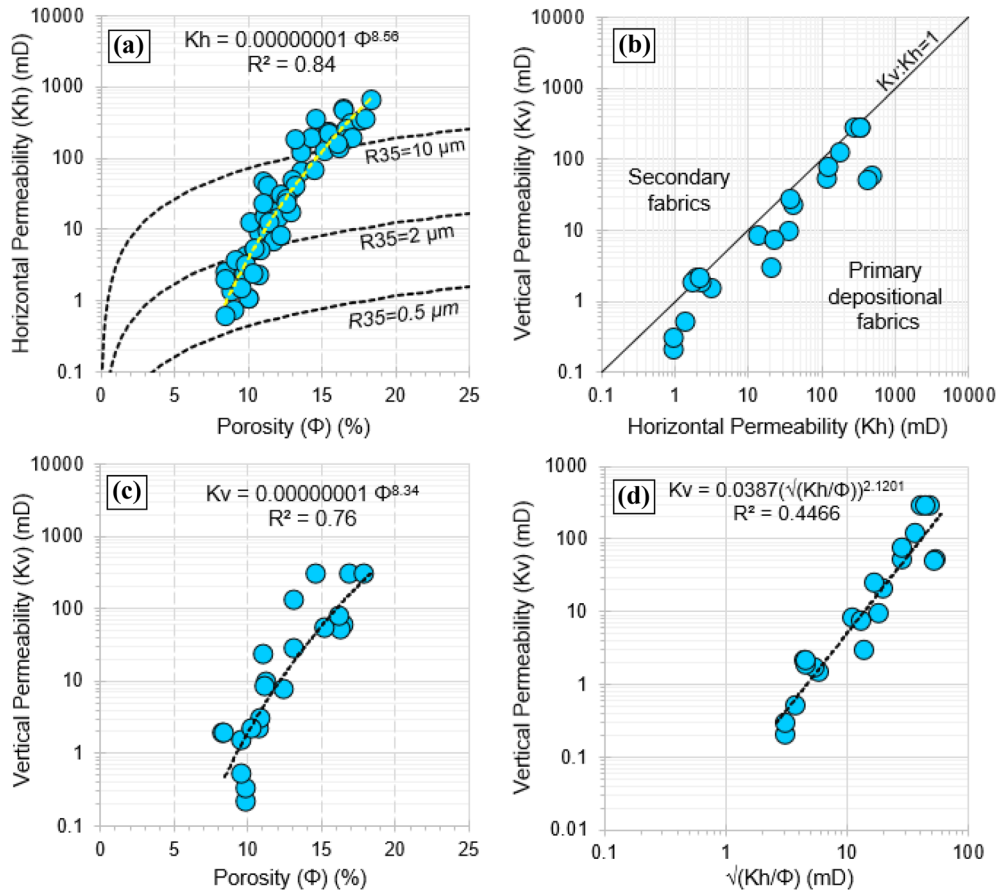


**Figure 24.** Relationships between core-measured (a) porosity ( $\Phi$ ) vs. horizontal permeability ( $K_h$ ); (b) vertical permeability ( $K_v$ ) vs.  $K_h$ ; (c)  $K_v$  vs.  $\Phi$ ; and (d)  $K_v$  vs. mean hydraulic radius ( $\sqrt{K_h/\Phi}$ ), illustrating the porosity–permeability characteristics of the Bahariya Formation. Data belong to Well AG-99. [1 mD (millidarcy) =  $9.86923 \times 10^{-16}$  meter<sup>2</sup>].

fair to good qualities while the glauconitic interval had poor quality in general ( $K_h < 1$  mD) in terms of porosity and permeability. However, the cored AR-E interval had high  $S_w$  and devoid of any net pay and, therefore, we recommend that the interval can be excluded from the completion strategy.

**Bahariya Reservoir**

The Bahariya Formation is the primary hydrocarbon producing clastic interval in the Abu Gharadig field along with the AR-G Member. A wide range of depositional environment is interpreted for the Bahariya Formation at various parts of the

Western Desert, including shallow marine, coastal, estuarine, lagoonal to fluvial/fluviodeltaic (Said, 1990; Darwish et al., 1994; Dominik, 1985; Abdel-Kireem et al., 1996; Catuneanu et al., 2006; El Beialy et al., 2008, 2010; El Atfy, 2011; Ghassal et al., 2018). In a recent study from the nearby Badr El Din-1 field, Farouk et al. (2021) deciphered a transgressive shelf-shoreface depositional environment. The studied Bahariya reservoir interval was composed of fine-grained massive sandstones with thin siltstone intercalations. The presence of rip-up clasts along with planar laminations and massive nature of the sandstone unit is indicative of rapid sediment discharge in a high energy environment (Sen et al., 2016; Dey and Sen, 2018; Sen and Dey, 2019, 2020;



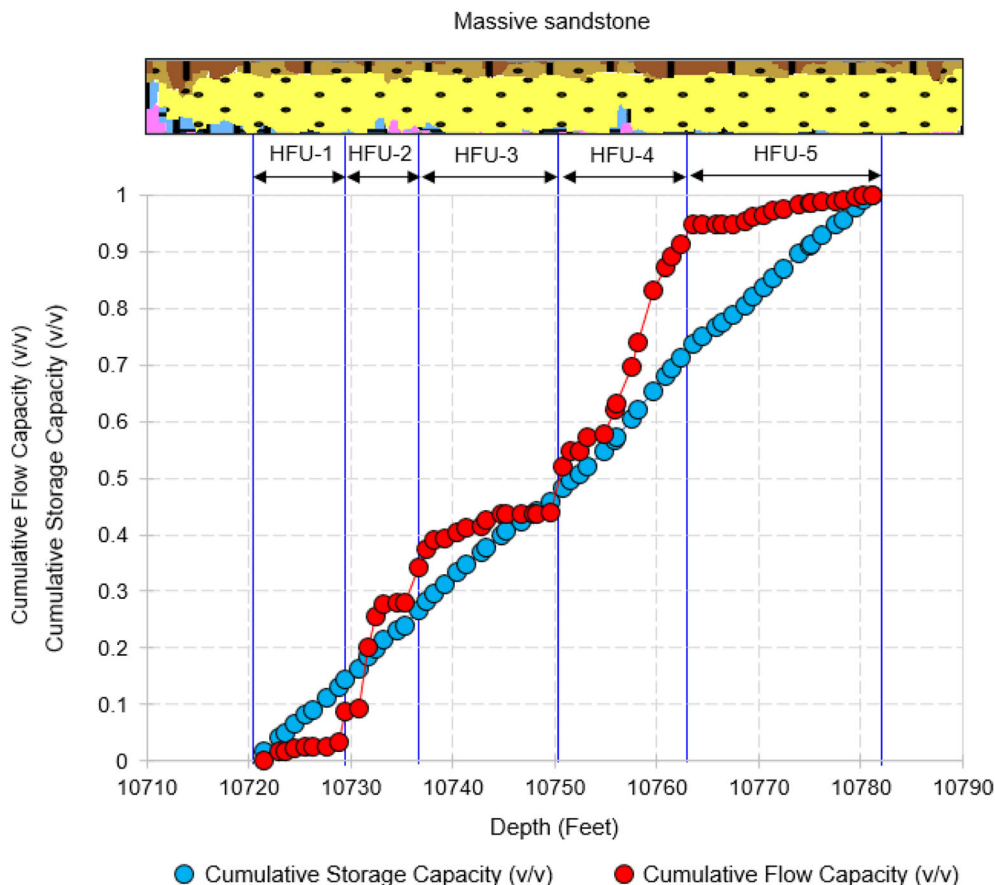


**Figure 25.** Stratigraphic modified Lorenz plots (SMLP) showing flow and storage capacities along with the various hydraulic flow units (HFU) within the Bahariya Formation in Well AG-99.

Baouche et al., 2020, 2021a; Mutebi et al., 2021) and refers to a channel system. The thin mud lamina/drapes are indicative of intermittent low energy conditions between the dominant sediment flux periods. We infer that the studied Bahariya Formation is a channel deposit in a coastal or fluvio-deltaic environment. The good porosity (average 13%) and superlative permeability (up to 649 mD with average of ~ 100 mD) of the interval indicate a very good quality reservoir (*FZI* up to 9  $\mu\text{m}$ ) and are typical characteristics of high energy channel deposits. It has preserved the primary depositional fabrics with isotropic pore system contributing to the storage capacity. The thin siltstone intercalations are associated with the lower end of the porosity-permeability distribution and may act as vertical permeability barriers along with the in-between shale layers.

The direct measurements in well AG-99 taken during September 2011 indicate that the Bahariya reservoir was depleted with present-day pore pressure slightly below the hydrostatic gradient (Khaldia Petroleum Company, 2013). In February 2013, a development well AG-109 was drilled near the studied well AG-99 and the well testing showed oil and gas production rates of 1264 BOPD<sup>10</sup> (barrel oil per day) and 1.9 MMSCFD<sup>11</sup> (million standard cubic ft per day), respectively (Khaldia Petroleum Company, 2013). Being fine- to medium-grained, moderately cemented, the Bahariya sandstones may potentially yield sanding issues in future with continued production induced depletion. Also, a higher rate of depletion can increase the stress path value

<sup>10</sup> 1 bopd = 0.1589 cubic meter per day.

<sup>11</sup> 1 MMSCFD (million standard cubic ft/day) = 0.02832 MMSCMD (million standard cubic meter/day).

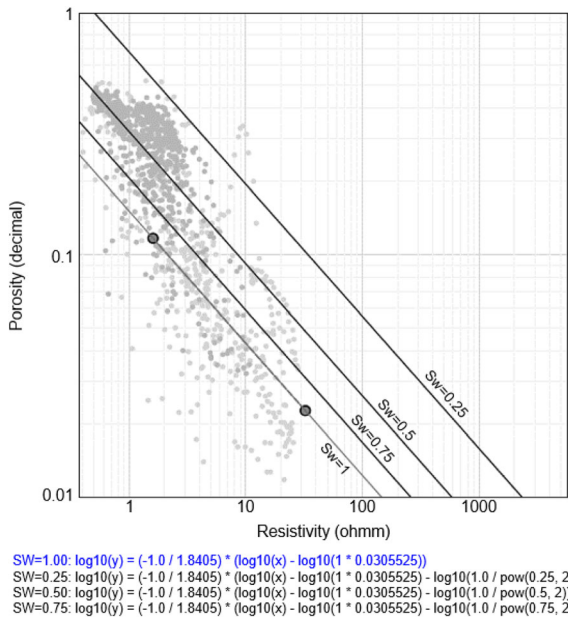


Figure 26. Pickett plot of Bahariya Formation in Well AG-99.

beyond the critical failure limit and incur normal faulting in the reservoir. To address these potential challenges, we recommend performing a geomechanical assessment to understand its vulnerability and design an effective production management, completion and sand control strategy.

### CONCLUSIONS

This work presents a comprehensive reservoir petrophysical assessment of the various lithofacies intervals in the Cenomanian Bahariya Formation and Turonian Abu Roash (AR-D and AR-E) Members in the Abu Gharadig field. The distribution and variation of the key petrophysical properties across the various lithofacies within a single formation have critical effects on reservoir deliver-

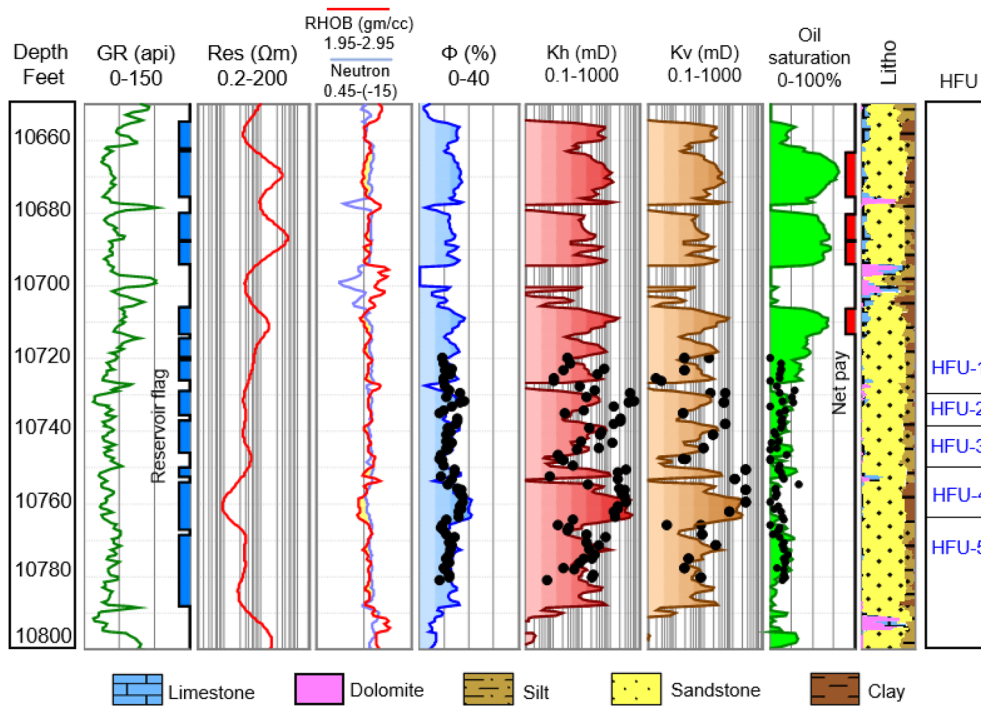
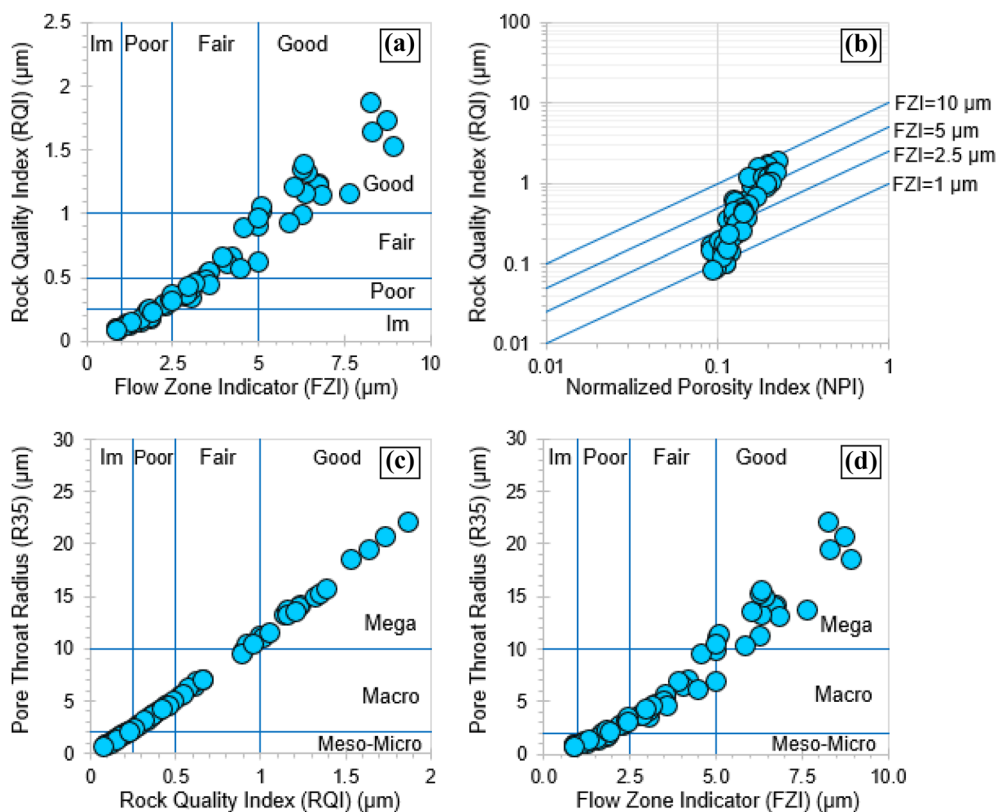


Figure 27. Vertical distribution of lithologic and petrophysical properties within the Bahariya Formation in the Well AG-99. Black dots indicate the core measurements. [1 ft = 0.3048 m; 1 mD (millidarcy) =  $9.86923 \times 10^{-16}$  meter<sup>2</sup>].



**Figure 28.** Characterization of the Bahariya Formation. Plots of *RQI* vs. (a) *FZI* and (b) *NPI*. Estimated pore throat radius (*R35*) is plotted against (c) *RQI* and (d) *FZI*. Data belong to Well AG-117. ‘Im’ indicates ‘impervious’ quality of the reservoir. Ranks used in (a), (c) and (d) are classified following Nabawy and Al-Azazi (2015).

ability and its development strategy. The availability of an extensive core dataset provided us the opportunity to infer the various reservoir storage and flow parameters. We conclude that the Bahariya sandstone reservoir consists of macro- and megaposity and exhibit isotropic pore system, but the cored interval has very high water saturation. The AR-E clastics have fair qualities. Within the AR-E, the calcareous sandstone intervals have higher porosity and permeability than the associated glauconitic siltstone layers; however, both lithofacies are water-saturated. Apart from these two intervals, we also assessed the AR-D carbonate interval. The limestone lithofacies contributes to most of the storage space and flow capacity of the AR-D

Member, while the argillaceous intervals are very tight. Overall, the AR-D appears to be impervious to poor and that necessitates a suitable stimulation strategy to develop the net pay zone in the LS lithofacies. However, a recently drilled well exhibited promising well test results from the tight AR-D Member. Therefore, the presented reservoir characterization and discussed field development recommendations will aid in optimizing the further planning. This core-based work is limited to the well scale and future work will attempt a three dimensional geomodelling to infer the field wide distribution of interpreted reservoir properties and its lateral variability affecting reservoir quality.

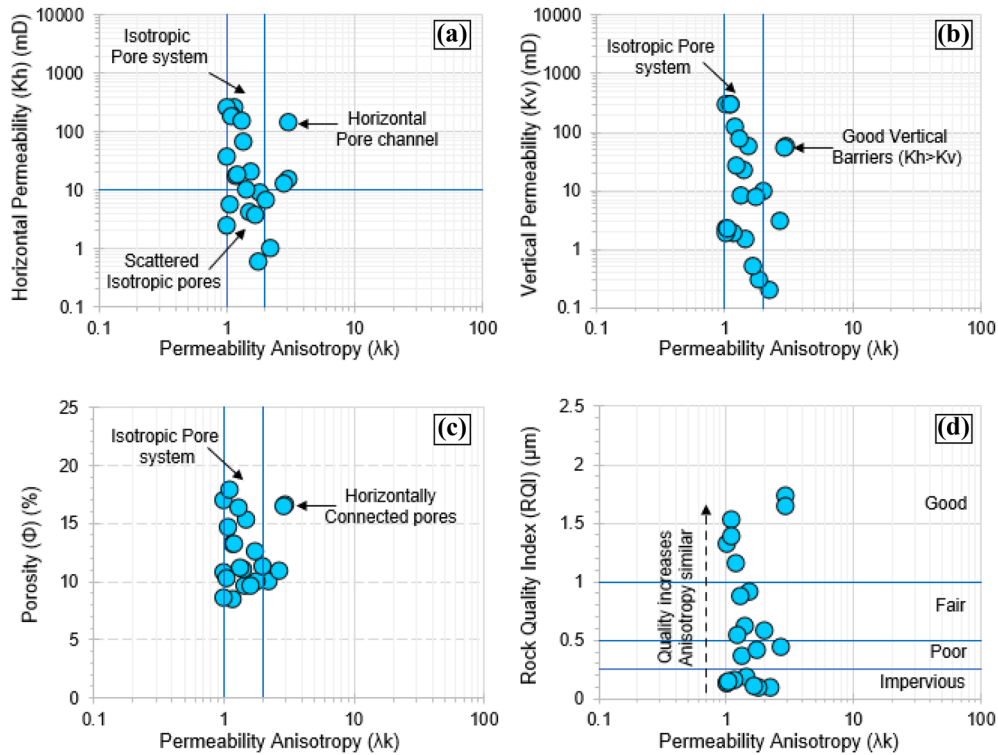


**Figure 29.** Interpretation of flow characteristics of the Bahariya Formation by plotting permeability anisotropy ( $\lambda k$ ) against (a) horizontal permeability ( $K_h$ ), (b) vertical permeability ( $K_v$ ), (c) porosity ( $\Phi$ ) and (d)  $RQI$ . Data belong to Well AG-99. [1 mD (millidarcy) =  $9.86923 \times 10^{-16}$  meter<sup>2</sup>].

**Table 4.** Summary of the core-based petrophysical properties of the Bahariya reservoir based on the core measurements.

Petrophysical characteristics	Bahariya sandstones with siltstone intercalations			
	Min	Max	Avg	CV
Porosity ( $\Phi$ ) (%)	8.42	18.4	12.61	0.216
Horizontal Permeability ( $K_h$ ) (mD)	0.58	649.6	95.53	1.478
Vertical Permeability ( $K_v$ ) (mD)	0.2	285	58.49	1.644
$K_v/K_h$	0.109	0.966	0.528	0.546
Permeability Anisotropy ( $\lambda k$ )	1.017	3.02	1.614	0.392
Mean Hydraulic Radius (mD)	2.602	59.413	19.466	0.789
Grain Density (gm/cc)	2.63	2.69	2.655	0.005
Rock Quality Index ( $RQI$ ) ( $\mu m$ )	0.082	1.866	0.611	0.789
Normalized Porosity Index ( $NPI$ )	0.092	0.226	0.145	0.249
Flow Zone Indicator ( $FZI$ ) ( $\mu m$ )	0.876	8.905	3.74	0.602
Pore Throat Radius ( $R_{35}$ ) ( $\mu m$ )	0.668	22.058	6.659	0.868

‘Avg’ and ‘CV’ refer to the average values and coefficient of variation [1 mD (millidarcy) =  $0.986923 \times 10^{-15}$  meter<sup>2</sup>]

**ACKNOWLEDGMENTS**

Authors express their sincere gratitude to Professor John Carranza (Editor-in-Chief) and the four reviewers for their constructive reviews which benefited our work. The authors are grateful to Egyp-

tian General Petroleum Corporation (EGPC) for the dataset and the permission to publish this study. Interpretation presented in this paper is solely of the authors and does not necessarily reflect their respective organizations.



## AUTHORS CONTRIBUTIONS

SF and SS were involved in conceptualization; SF, SS and HA contributed to methodology, formal analysis and investigation; SS contributed to the writing-original draft preparation; SF supervised the project. All authors were involved in writing-review and editing. All authors read and approved the final manuscript.

## FUNDING

No funding was received for conducting this study.

## DATA AVAILABILITY

The datasets generated during and/or analyzed during the current study are not publicly available due restricted permissions but are available from the corresponding author on reasonable request.

## DECLARATIONS

**Conflict of Interest** The authors have no competing interest to declare that are relevant to the content of this article.

## REFERENCES

- Abdel-Fattah, M. I., Sen, S., Abuzied, S. M., Abioui, M., Radwan, A. E., & Benssaou, M. (2022). Facies analysis and petrophysical investigation of the Late Miocene Abu Madi sandstone gas reservoirs from offshore Baltim East field (Nile Delta, Egypt). *Marine and Petroleum Geology*, *137*, 105501.
- Abdel-Kireem, M. R., Schrank, E., Samir, A. M., & Ibrahim, M. I. A. (1996). Cretaceous palaeoecology, palaeogeography and palaeoclimatology of the northern Western Desert Egypt. *Journal of African Earth Sciences*, *22*, 93–112.
- Abdelmaksoud, A., Amin, A. T., El-Habaak, G. H., & Ewida, H. F. (2019a). Facies and petrophysical modeling of the Upper Bahariya Member in Abu Gharadig oil and gas field, north Western Desert Egypt. *Journal of African Earth Sciences*, *149*, 503–516.
- Abdelmaksoud, A., Ewida, H. F., El-Habaak, G. H., & Amin, A. T. (2019b). 3D structural modeling of the Upper Bahariya Member in Abu Gharadig oil and gas field, North Western Desert Egypt. *Journal of African Earth Sciences*, *150*, 685–700.
- Abuamarah, B. A., & Nabawy, B. S. (2021). A proposed classification for the reservoir quality assessment of hydrocarbon-bearing sandstone and carbonate reservoirs: A correlative study based on different assessment petrophysical procedures. *Journal of Natural Gas Science and Engineering*, *88*, 103807.
- Abuamarah, B. A., Nabawy, B. S., Shehata, A. M., Kassem, O. M. K., & Ghrefat, H. (2019). Integrated geological and petrophysical characterization of Oligocene deep marine unconventional poor to tight sandstone gas reservoir. *Marine and Petroleum Geology*, *109*, 868–885.
- Abuseda, H., Fathy, M., & Elnaggar, O. M. (2021). Impact of sedimentologic diagenesis on the petrophysical evaluation of the reservoir rocks in BED-1 field, Western Desert Egypt. *Asian Journal of Geological Research*, *4*(2), 45–53.
- Adly, O., El Araby, A. M., El Barkooky, A., Abu Roash F. (2016). Member as a potential self-sourced reservoir in Abu Gharadig Basin, Western Desert of Egypt. In: AAPG Hedberg Conference, The Future of Basin and Petroleum Systems Modeling, Santa Barbara, California, April 3–8. Search and Discovery Article #90257.
- Al-Hajeri, S. K., Ayoub, M. R., Al Shehhi, A. S., Negahban, S., Riberio, M. T., Bahamaish, J. N., (2007). Tight reservoirs – A development challenge example from a carbonate reservoir offshore Abu Dhabi. In: SPE Middle East Oil and Gas Show and Conference, Manama, Bahrain, March 11–14. SPE-105420-MS.
- Alsharhan, A., & Sadd, J. L. (2000). Stylolites in Lower Cretaceous carbonate reservoirs UAE. In A. S. Alsharhan & R. W. Scott (Eds.), *Middle east models of jurassic/cretaceous carbonate system* (pp. 185–207). Tulsa: Society for Sedimentary Geology Special Publication.
- Alyan, M., Martin, J., Irwin, D., (2015). Field development plan optimization for tight carbonate reservoirs. In: SPE Abu Dhabi International Petroleum Exhibition and Conference, Abu Dhabi, UAE, Nov 9–12. SPE-177695-MS.
- Amaefule, J., Altunbay, M., Tiab, D., Kersey, D., Keelan, D., (1993). Enhanced reservoir description, using core and log data to identify hydraulic (flow) units and predict permeability in uncored intervals/wells. SPE Annual Technical Conference and Exhibition, Houston, Texas. SPE 26436.
- Apex International Energy, (2021). Press release, 18 Jan, Cairo, Egypt. <https://apexintl.com/blue-water-energy-llp-to-partner-with-apex-international-energy-2/>.
- Archie, G. E. (1942). The electrical resistivity log as an aid in determining some reservoir characteristics. *Journal of Petroleum Technology*, *5*, 54–62.
- Baioumy, H., & Boulis, S. (2012). Glauconites from the Bahariya Oasis: An evidence for Cenomanian marine transgression in Egypt. *Journal of African Earth Sciences*, *70*, 1–7.
- Banerjee, S., Mondal, S., Chakraborty, P. P., & Meena, S. S. (2015). Distinctive compositional characteristics and evolutionary trend of Precambrian glaucony: Example from Bhalukona Formation, Chhattisgarh basin, India. *Precambrian Research*, *271*, 33–48.
- Banerjee, S., Bansal, U., & Thorat, A. V. (2016a). A review on palaeogeographic implications and temporal variation in glaucony composition. *Journal of Paleogeography*, *5*, 43–71.
- Banerjee, S., Bansal, U., Pande, K., & Meena, S. S. (2016). Compositional variability of glauconites within the Upper Cretaceous Karai Shale Formation, Cauvery Basin, India: Implications for evaluation of stratigraphic condensation. *Sedimentary Geology*, *331*, 12–29.
- Banerjee, S., Farouk, S., Nagm, E., Choudhury, T. R., & Meena, S. S. (2019). High Mg-glaucinite in the Campanian Duwi Formation of Abu Tartur Plateau, Egypt and its implications. *Journal of African Earth Sciences*, *156*, 12–25.
- Bansal, U., Banerjee, S., Ruidas, D. K., & Pande, K. (2018). Origin and geochemical characterization of the glauconites in the upper cretaceous Lameta formation, Narmada basin, central India. *Journal of Paleogeography*, *7*, 99–116.
- Bansal, U., Banerjee, S., Pande, K., & Ruidas, D. K. (2019). Unusual seawater composition of the Late Cretaceous Tethys

- imprinted in glauconite of Narmada basin Central India. *Geological Magazine*, 157, 233–247.
- Baouche, R., Sen, S., Debiante, K., & Ganguli, S. S. (2020). Integrated reservoir characterization of the Paleozoic and Mesozoic sandstones of the El Ouar field, Algeria. *Journal of Petroleum Science and Engineering*, 194, 107551.
- Baouche, R., Sen, S., Ganguli, S. S., & Ferial, H. A. (2021a). Petrophysical, geomechanical and depositional environment characterization of the Triassic TAGI reservoir from the Hassi Berkine South field, Berkine Basi, Southeastern Algeria. *Journal of Natural Gas Science and Engineering*, 92, 104002.
- Baouche, R., Sen, S., Ganguli, S. S., & Boutaleb, K. (2021). Petrophysical and geomechanical characterization of the Late Cretaceous limestone reservoirs from the Southeastern Constantine Basin Algeria. *Interpretation*, 9(4), SH1–SH9.
- Barbier, M., Hamon, Y., Callot, J.-P., Floquet, M., & Daniel, J.-M. (2012). Sedimentary and diagenetic controls on the multiscale fracturing pattern of a carbonate reservoir: The Madison Formation (Sheep Mountain, Wyoming, USA). *Marine and Petroleum Geology*, 29(1), 50–67.
- Baud, P., Meredith, P. G., & Townend, E. (2012). Permeability evolution during triaxial compaction of an anisotropic porous sandstone. *Journal of Geophysical Research*, 117, B05203. <https://doi.org/10.1029/2012JB009176>.
- Bosworth, W., El-Hawat, A. S., Helgeson, D. E., & Burke, K. (2008). Cyrenaican “shock absorber” and associated inversion strain shadow in the collision zone of Northeast Africa. *Geology*, 36(9), 695–698.
- Boukhary, M., El Nahas, S., El Naby, A. A., Aal, M. H. A., Mahsoub, M., & Faris, M. (2014). Seismic and sequence stratigraphy of Upper Cretaceous-Tertiary succession, eastern Abu-Gharadig Basin, Western Desert Egypt. *Stratigraphy*, 11(2), 109–141.
- Burchette, T. P., & Wright, V. P. (1992). Carbonate ramp depositional systems. *Sedimentary Geology*, 79(1–4), 3–57.
- Catuneanu, O., Khalifa, M. A., & Wanas, H. A. (2006). Sequence stratigraphy of the Lower Cenomanian Bahariya Formation, Bahariya Oasis, Western Desert Egypt. *Sedimentary Geology*, 190, 121–137.
- Chimmalgi, V. S., Al-Humond, J., Al-Sabea, S., Gazi, N., Bardalaye, J., Mudavakkat, A., Al-Enezi, H., Al-Zankawi, O., Ahsan, J., Abdulrazzaq, E., Tirkey, N., Kotecha, R., Snasiri, F., Jalan, S., Al-Zabbi, R., Al-Dousari, M., Al-Othman, M., Al-houti, N., Benamer, N., Elsherif, T., Surjaatmadja, J., Elmofiti, M., (2013). Reactivating a tight carbonate reservoir in the Greater Burgan Field: Challenges, options and solutions. In: SPE Middle East Oil and Gas Show and Conference, Manama, Bahrain, March 10–13. SPE-164248-MS.
- Darwish, M., Abu Khadrah, A. M., Abdel Hamid, M. L., Hamed, T. A. (1994). Sedimentology, environmental conditions and hydrocarbon habitat of the Bahariya Formation, central Abu Gharadig Basin, Western Desert, Egypt. Proceedings of the 12th Petroleum Exploration and Production Conference, Cairo, Egypt, Nov 12–15.
- Dey, J., & Sen, S. (2018). Sequence stratigraphic model of Middle Permian Barakar Formation from a Marginal Gondwana Basin, India. *Journal of Earth Science*, 29, 745–754.
- Dominik, W. (1985). Stratigraphie und Sedimentologie (Geochemie, Schwermineralanalyse) der Oberkreide von Bahaiya und ihre Korrelation zum Dakhla-Becken (Western Desert, Ägypten). *Berliner geowissenschaftliche Abhandlungen A* 62 p. 173.
- Egyptian General Petroleum Corporation (EGPC). (1992). Western Desert oil and gas fields: A comprehensive overview.
- Egyptian General Petroleum Corporation (EGPC). (2019). Production: Whole Drilling Report.
- Egypt Upstream Gateway (EUG). (2021). 2021 Bid Round Highlights. <https://eug.petroleum.gov.eg/>.
- El Atfy, H. (2011). *Cretaceous palynology of the GPTSW-7 Well, Western Desert Egypt*. LAP LAMBERT Academic Publishing GmbH & Co.
- El Beialy, S. Y., El Atfy, H. S., El Khoriby, E. M., & Abu-Zied, R. H. (2008). Palynostratigraphy, palynofacies and the source rock evaluation of the Cenomanian Bahariya Formation, GPTSW-7 well, north Western Desert Egypt. *Journal of Environmental Science*, 36, 63–88.
- El Beialy, S. Y., El Atfy, H. S., Zavada, M. S., El Khoriby, E. M., & Abu-Zied, R. H. (2010). Palynological, palynofacies, paleoenvironmental and organic geochemical studies on the Upper Cretaceous succession of the GPTSW-7 well, north Western Desert Egypt. *Marine and Petroleum Geology*, 27, 370–385.
- El Gazzar, A. M., Moustafa, A. R., & Bentham, P. (2016). Structural evolution of the Abu Gharadig field area, Northern Western Desert Egypt. *Journal of African Earth Sciences*, 124, 340–354.
- El Sharawy, M. S., & Nabawy, B. S. (2016). Determination of electrofacies using wireline logs based on multivariate statistical analysis for the Kareem Formation, Gulf of Sues. *Egypt. Environmental Earth Sciences*, 75, 1394.
- El Sharawy, M. S., & Nabawy, B. S. (2019). Integration of electrofacies and hydraulic flow units to delineate reservoir quality in Uncored reservoirs: A case study, Nubia sandstone reservoir, Gulf of Suez. *Egypt. Natural Resources Research*, 28, 1587–1608.
- Elhossainy, M. M., Abdelmaksoud, A., Ali, M., & Alrefaee, H. A. (2021). Integrated sedimentological and petrophysical characterization of the Lower Cenomanian clastic Bahariya reservoir in Abu Gharadig Basin, Western Desert. *Egypt. Journal of African Earth Sciences*, 184, 104380.
- Farouk, S. (2015). Upper Cretaceous sequence stratigraphy of the Galala Plateaux, Western side of the Gulf of Suez Egypt. *Marine and Petroleum Geology*, 60, 136–158.
- Farouk, S., Sen, S., Ganguli, S. S., Abuseda, H., & Debnath, A. (2021). Petrophysical assessment and permeability modeling utilizing core data and machine learning approaches – A study from the Badr El Din-1 field Egypt. *Marine and Petroleum Geology*, 133, 105265.
- George, B. K., Clara, C., Al Mazrooei, S., Manseur, S., Abdou, M., Chong, T. S., Al Raeesi, M., (2012). Challenges and key learning for developing tight carbonate reservoirs. In: Abu Dhabi International Petroleum Exhibition and Conference (ADIPEC), Abu Dhabi, UAE, Nov 11–14. SPE 161693. <https://doi.org/10.2118/161693-MS>.
- Ghassal, B. I., Littke, R., Atfy, H. E., Sindern, S., & Scholtysik, G. (2018). Source rock potential and depositional environment of Upper Cretaceous sedimentary rocks, Abu Gharadig Basin, Western Desert, Egypt: An integrated palynological, organic and inorganic geochemical study. *International Journal of Coal Geology*, 186, 14–40.
- Gingras, M. K., MacMillan, B., & Balcom, B. J. (2002). Visualizing the internal physical characteristics of carbonate sediments with magnetic resonance imaging and petrography. *Bulletin of Canadian Petroleum Geology*, 50, 363–369.
- Guiraud, R. (1998). Mesozoic rifting and basin inversion along the Northern African Tethyan margin: An overview. *Geological Society, London, Special Publications*, 132(1), 217–229.
- Guiraud, R., & Bosworth, W. (1997). Senonian basin inversion and rejuvenation of rifting in Africa and Arabia: Synthesis and implications to plate-scale tectonics. *Tectonophysics*, 282(1–4), 39–82.
- Guiraud, R., & Maurin, J. C. (1992). Early cretaceous rifts of Western and Central Africa: An overview. *Tectonophysics*, 213(1–2), 153–168.
- Guiraud, R., Bosworth, W., Thierry, J., & Delplanque, A. (2005). Phanerozoic geological evolution of Northern and Central

- Africa: An overview. *Journal of African Earth Science*, 43(1–3), 83–143.
- Gunter, G. W., Finneran, J. M., Hartmann, D. J., Miller, J. D., (1997). Early determination of reservoir flow units using an integrated petrophysical method. In: SPE Annual Technical Conference and Exhibition, SPE-38679, pp. 373–380.
- Guo, G., Diaz, M. A., Paz, F. J., Smalley, J., & Waninger, E. A. (2007). Rock typing as an effective tool for permeability and water-saturation modeling: A case study in a clastic reservoir in the Oriente Basin. *SPE Reservoir Evaluation & Engineering*, 10(6), 730–739.
- Harris, N. B. (2006). Low-porosity haloes at stylolites in the feldspathic Upper Jurassic Ula sandstone, Norwegian North Sea: An integrated petrographic and chemical mass-balance approach. *Journal of Sedimentary Research*, 76, 444–459.
- Heap, M. J., Baud, P., Reuschlé, T., & Meredith, P. G. (2014). Stylolites in limestones: Barriers to fluid flow? *Geology*, 42(1), 51–54.
- Hewaidy, A. G., Elshahat, O. R., & Kamal, S. (2018). Stratigraphy, facies analysis and depositional environments of the Upper Unit of Abu Roash “E” member in the Abu Gharadig field, Western Desert Egypt. *Journal of African Earth Sciences*, 139, 26–37.
- Kassab, M. A., Abbas, A. E., & Attiya, A. S. (2019). Hydrocarbon potential of Upper Bahariya member in Um Baraka oil field, North Western Desert Egypt. *Journal of Astronomy and Geophysics*, 8(1), 204–219.
- Khalda Petroleum Company, (2013). Well completion reports of AG-108 and AG-109, internal reports.
- Khaled, K. A. (1999). Cretaceous Source rocks at the Abu Gharadig oil- and gasfield, Northern Western Desert Egypt. *Journal of Petroleum Geology*, 22(4), 377–395.
- Koehn, D., Rood, M. P., Beaudoin, N., Bons, P. D., & Gomez-Rivas, E. (2016). A new stylolite classification scheme to estimate compaction and local permeability variation. *Sedimentary Geology*, 346, 60–71.
- Kolodzie, S., (1980). Analysis of pore throat size and use of the Waxman–Smits equation to determine OOIP in Spindle Field, Colorado. Proceedings Society of Petroleum Engineers, 55th Annual Technical Fall Conference, SPE-9382.
- Latief, A. I., Syofyan, S., Ab Hamid, T. M. T., Al Amoudi, M. A., Shabibi, T. A., (2019). Unlocking tight carbonate reservoir potential: Geological characterization to execution. In: SPE Middle East Oil and Gas Show and Conference, Manama, Bahrain, March 18–21. SPE-194712-MS.
- Lind, I., Nykjaer, O., Priihsolm, S., & Springer, N. (1994). Permeability of stylolite-bearing chalk. *Journal of Petroleum Technology*, 46, 986–993.
- Lotfy, H. I. (1984). *A geophysical study on the Qattara Depression Area, Western Desert*. Thesis, El Minya University, Egypt.
- Mahmoud, H., Lotfy, H., & Bakr, A. (2019). A structural evolution of JG and JD fields, Abu Gharadig basin, Western Desert, Egypt, and its impact on hydrocarbon exploration. *Journal of Petroleum Exploration and Production Technology*, 9, 2555–2571.
- Mansour, A., Gentzis, T., Wagreich, M., Tahoun, S. S., & Elewa, A. M. T. (2020). Short-term sea level changes of the Upper Cretaceous Carbonates: Calibration between palynomorphs composition, inorganic geochemistry, and stable isotopes. *Minerals*, 10, 1099.
- Moustafa, A. R., (2008). Mesozoic-Cenozoic basin evolution in the Northern Western Desert of Egypt. In: Salem, M., El-Arnauti, A., Saleh, A. (eds) 3rd Symposium on the Sedimentary Basins of Libya, The Geology of East Libya, vol. 3, pp. 29–46.
- Moustafa, A. R. (2013). Fold-related faults in the Syrian Arc belt of northern Egypt. *Marine and Petroleum Geology*, 48, 441–454.
- Mutebi, S., Sen, S., Sserubiri, T., Rudra, A., Ganguli, S. S., & Radwan, A. E. (2021). Geological characterization of the Miocene-Pliocene succession in the Semliki Basin, Uganda: Implications for hydrocarbon exploration and drilling in the East African Rift System. *Natural Resources Research*, 30, 4329–4354.
- Nabawy, B. S., & Al-Azazi, N. A. (2015). Reservoir zonation and discrimination using the routine core analyses data: The upper Jurassic Sabatayn sandstones as a case study, Sabatayn basin. *Yemen. Arabian Journal of Geosciences*, 8(8), 5511–5530.
- Nabawy, B. S., Sediek, K. N., & Nafee, S. A. (2015). Pore fabric assignment using electrical conductivity of some Albian-Cenomanian sequences in north Eastern Desert Egypt. *Arabian Journal of Geosciences*, 8(8), 5601–5615.
- Nabawy, B. S., Rashed, M. A., Mansour, A. S., & Affify, W. S. M. (2018). Petrophysical and microfacies analysis as a tool for reservoir rock typing and modeling: Rudeis Formation, offshore October Oil Field, Sinai. *Marine and Petroleum Geology*, 97, 260–276.
- Pickett, G. R. (1966). A review of current techniques for determination of water saturation from logs. *Journal of Petroleum Technology*, 18(11), 1425–1433.
- Rizk, M., Rafik, M., El-Behairy, A., Abdel-Nabi, M., (2013). Effect of petrophysical re-interpretation on matured field’s development planning and producing reserves boosting up in Abu El Gharadig Basin, Western Desert, Egypt. In: SPE North Africa Technical Conference & Exhibition, Cairo, Egypt, April 15–17. SPE-164701.
- Said, R. (1990). The Geology of Egypt. A.A. Balkema, Rotterdam, Brookfield pp 729.
- Salamy, S. P., Al-Mubarak, H. K., Hembling, D. E., Al-Ghamdi, M. S., (2006). Deployed smart technologies enablers for improving well performance in tight reservoirs-case: Shaybah Field, Saudi Arabia. In: Intelligent Energy Conference and Exhibition, Amsterdam, The Netherlands, April 11–13. SPE 99281. <https://doi.org/10.2118/99281-MS>.
- Sarhan, M. A. (2017). Wrench tectonics of Abu Gharadig Basin, Western Desert, Egypt: A structural analysis for hydrocarbon prospects. *Arabian Journal of Geosciences*, 10, 399.
- Sarhan, M. A. (2021). Geophysical appraisal for the sandy levels within Abu Roash C and E members in Abu Gharadig Field, Western Desert Egypt. *Journal of Petroleum Exploration and Production*, 11, 1101–1122.
- Sarhan, M. A., & Collier, R. E. (2018). Distinguishing rift-related from inversion-related anticlines: Observations from the Abu Gharadig and Gindi Basins, Western Desert Egypt. *Journal of African Earth Sciences*, 145, 234–245.
- Sarhan, M. A., Basal, A. M. K., & Ibrahim, I. M. (2017a). Integration of seismic interpretation and well logging analysis of Abu Roash D Member, Gindi Basin, Egypt: Implication for detecting and evaluating fractured carbonate reservoirs. *Journal of African Earth Sciences*, 135, 1–13.
- Sarhan, M. A., Basal, A. M. K., & Ibrahim, I. L. (2017b). Seismic and well logging interpretation for evaluation of the lower Bahariya reservoir, southwest Qarun (SWQ) Field, Gindi Basin Egypt. *Marine Geophysical Research*, 38, 271–290.
- Sen, S., & Dey, J. (2019). A field-scale overview of facies architectures and depositional environment integrating core and geophysical log data: Study from a Marginal Gondwana Basin, India. *Journal of the Geological Society of India*, 94, 238–244.
- Sen, S., & Dey, J. (2020). Cyclic sedimentation in the Barakar Formation of the Karanpura Field, Marginal Gondwana Basin, India. *Journal of the Geological Society of India*, 95, 293–300.
- Sen, S., Das, N., & Maiti, D. (2016). Facies analysis and depositional model of late Permian Raniganj formation: Study from

- Raniganj coal bed methane block. *Journal of the Geological Society of India*, 88, 503–516.
- Sen, S., Abioui, M., Ganguli, S. S., Elsheikh, A., Debnath, A., Benssaou, M., & Abdelhady, A. A. (2021). Petrophysical heterogeneity of the early Cretaceous Alamein dolomite reservoir from North Razzak oil field, Egypt integrating well logs, core measurements, and machine learning approach. *Fuel*, 306, 121698.
- Serra, O. (1988). *Fundamentals of well-log interpretation. 1. The acquisition of logging data* (3rd ed.). Elsevier.
- Slatt, R. (2006). Stratigraphic reservoir characterization for petroleum geologists, geophysicist and engineers. *Handbook of Petroleum Exploration and Production*, 6, 177–186.
- Winland, H. D. (1972). Oil accumulation in response to pore size changes, Weyburn Field, Saskatchewan. Amoco Production Research Report. F72-G-25.
- Zobaa, M. K., Oboh-Ikuenobe, F. E., & Ibrahim, M. I. (2011). The Cenomanian/Turonian oceanic anoxic event in the Razzak Field, North Western Desert, Egypt: Source rock potential and paleoenvironmental association. *Marine and Petroleum Geology*, 28, 1475–1482.